Journal of Human Evolution 169 (2022) 103211

Contents lists available at ScienceDirect

Journal of Human Evolution

journal homepage: www.elsevier.com/locate/jhevol

A refined chronology for the Middle and early Upper Paleolithic sequence of Riparo Mochi (Liguria, Italy)

Marine Frouin [a, b, *], Katerina Douka [c, d, *], Aditi Krishna Dave [e], Jean-Luc Schwenninger [b], Norbert Mercier [f], Andrew S. Murray [g], Fabio Santaniello [h, i], Giovanni Boschian [j, k], Stefano Grimaldi [h, i], Thomas Higham [c, d, l]

[a] Department of Geosciences, Stony Brook University, 255 Earth and Space Sciences Building (ESS), Stony Brook, NY 11794-2100, USA
[b] Research Laboratory for Archaeology and the History of Art, University of Oxford, 1–2 South Parks Road, Oxford OX1 3TG, United Kingdom
[c] Department of Evolutionary Anthropology, Faculty of Life Sciences, University of Vienna, Djerassiplatz 1, Vienna, Austria
[d] Human Evolution and Archaeological Sciences (HEAS), University of Vienna, A-1030, Vienna, Austria
[e] Department of Geosciences, University of Tübingen, Schnarrenbergstrasse 94-96, 72076 Tübingen, Germany
[f] Archéosciences Bordeaux, UMR 6034 CNRS - Université Bordeaux Montaigne, Maison de l'archéologie, 33600 Pessac, France
[g] The Nordic Laboratory for Luminescence Dating, Department of Geoscience, Aarhus University and DTU Physics, DTU Risø Campus, DK-4000 Roskilde, Denmark
[h] Dipartimento di Lettere e Filosofia, Università di Trento, Trento, Italy
[i] Istituto Italiano di Paleontologia Umana, Anagni, Italy
[j] Dipartimento di Biologia, Università di Pisa, Pisa, Italy
[k] Palaeo-Research Institute, University of Johannesburg, P.O. Box 524, Auckland Park, 2006, South Africa
[l] Oxford Radiocarbon Accelerator Unit, Research Laboratory for Archaeology and the History of Art, University of Oxford, 1 South Parks Road, Oxford OX1 3TG, United Kingdom

ARTICLE INFO

Article history:
Received 26 January 2020
Accepted 22 April 2022
Available online xxx

Keywords:
Middle Paleolithic
Upper Paleolithic
Luminescence dating
Radiocarbon dating
Chronology
Bayesian modeling

ABSTRACT

The Riparo Mochi rock shelter, located on the Ligurian coast of Italy, is one of the most important early Upper Paleolithic sites on the Mediterranean rim. Its ~10-m-deep stratigraphy comprises a Mousterian sequence, followed by various development stages of the Upper Paleolithic. A series of radiometric dates on marine shells bearing traces of human modification has provided a chronological framework for the final Mousterian and the Proto-Aurignacian of the site. Based on modeling results, the end of the Mousterian was dated between 44.0 and 41.8 ka cal BP (68% probability) and the beginning of the Proto-Aurignacian between 42.7 and 41.6 ka cal BP (68% probability). However, these estimates were based on a limited number of radiocarbon ages in the Mousterian levels. Here, we report new dating of the Mochi sequence using luminescence techniques, along with new radiocarbon measurements. The combination of these results using a Bayesian modeling approach allows for the first time the establishment of a more precise timing for the Mousterian occupation at the site. We show that Mousterian groups were already present at Riparo Mochi by at least 65 ka and continued to occupy the site for another 20 ka. The transition to the earliest Upper Paleolithic at the site is centered around 44.3–41.1 ka (95.4% probability), providing our best age estimate for the beginning of the Early Upper Paleolithic and the establishment of modern human groups in the Balzi Rossi. The sequence continues upward with a more evolved Aurignacian phase and a Gravettian phase starting at ~26 ka or earlier.

1. Introduction

The transition from the Middle to the Upper Paleolithic (MP and UP, respectively) was marked by the disappearance of Neanderthals and the dispersion of anatomically modern humans across Eurasia. A variety of hypotheses have been proposed to explain why this transition happened, such as competition (Banks et al., 2008),

* Corresponding authors.
E-mail addresses: marine.frouin@stonybrook.edu (M. Frouin), katerina.douka@univie.ac.at (K. Douka).

https://doi.org/10.1016/j.jhevol.2022.103211

interbreeding (Smith et al., 2005, Vaesen et al., 2019), and/or abrupt environmental changes (Timmermann 2020). Understanding the causes and processes leading to the disappearance of Neanderthals and the spatial pattern of interaction between the different human groups is strongly dependent on the chronological resolution of the period and the region of interest (Higham et al., 2014).

The Liguro-Provençal arc between France and Italy comprises a concentration of sites preserving both late MP and early UP archaeological assemblages (Fig. 1) and holds great potential for understanding the relationship between Neanderthals, before their disappearance, and early modern humans as they dispersed into Europe (e.g., Conard and Bolus, 2003; Bietti and Negrino, 2007; Porraz and Negrino, 2008; Porraz et al., 2010; Anderson et al., 2015; Rossoni-Notter et al., 2016). The Riparo Mochi rock shelter, located on the Ligurian coast (Fig. 1), provides a well-preserved stratigraphic sequence spanning the MP and early UP. The site has been used as the type-site for defining the Proto-Aurignacian technocomplex in Europe (Laplace, 1977) and the development of the UP, with the Proto-Aurignacian likely to have given way to the Aurignacian, which was subsequently replaced by the Gravettian (Grimaldi et al., 2017; Santaniello and Grimaldi, 2019, 2020). Based on Bayesian modeling of previously published radiocarbon dates (Douka et al., 2012), the earliest Proto-Aurignacian of Riparo Mochi was suggested to date between 44 and 41.8 ka cal BP (^{14}C calibrated years before AD 1950; 68% probability). However, this work was not able to determine the age of the Mousterian occupation of the site due to the lack of suitable material for radiocarbon dating and the limit of the radiocarbon dating method around 50 ka. Hence, the Mousterian part of the sequence at Riparo Mochi has remained undated.

Here, we report a series of new optically stimulated luminescence (OSL) ages for both the MP and early UP parts of the site. We directly dated sediments associated with archaeological remains and periods of human occupation by measuring the time elapsed since minerals such as quartz and feldspar grains within the deposits were last exposed to daylight. We combine the luminescence results with previous and some new radiocarbon dates from the UP units using Bayesian modeling to obtain a more complete and precise age estimate for the final Mousterian and early UP occurrences at the site. We also attempt to correlate the chronological framework for the occupational levels at Mochi with other nearby archaeological sites to gain insight into human behavior in this key region.

1.1. Site setting, stratigraphy, and archaeological context

Riparo Mochi (43°47′3.66″ N, 7°32′4.18″ E) is a shallow rock shelter located at the base of a broad dolomitic limestone cliff called the Balzi Rossi, near the Italian-French border, in the Italian province of Liguria in northeastern Italy (Fig. 1). The site is part of a complex of over 15 caves, rock shelters, and open-air sites, commonly known as the Grimaldi sites. For a description of the site, refer to the study by Douka et al. (2012).

Since its discovery in 1938 by A.C. Blanc and L. Cardini, Riparo Mochi has been extensively and systematically excavated. From 1938 to 1959, excavations were undertaken by Cardini and Blanc, along with A. Segre, in three areas: the east sector, the west sector, and the central trench (Fig. 2). In 1995, A. Bietti and his team reinvestigated the east sector, correlating the sediments and archaeological material with Cardini's work in 1959, and studied the unexcavated Mousterian units of the east sectors for the first time (Grimaldi and Santaniello, 2014). Since 2007, the site of Riparo Mochi has been investigated by S. Grimaldi and his team. Collections from the old excavation campaigns have been re-examined to understand human settlement dynamics, raw material procurement strategies, land-use practices, and adaptive response of humans to local environmental conditions and for developing a robust chronological framework for the site (Douka et al., 2012; Grimaldi and Santaniello, 2014, 2020; Grimaldi et al., 2014, 2017; Tomasso, 2014; Tejero and Grimaldi, 2015; Santaniello, 2016, Santaniello and Grimaldi, 2019, 2020).

The lithology and geomorphology of the east sector and central trench have been studied in detail to draw site-based paleoclimatic inferences from the region (Laplace, 1977; Palma di Cesnola, 1993; Douka et al., 2012). The present stratigraphy is a ~10-m-deep profile that groups nine macro-units, labeled Unit A-I, from top to bottom (Table 1; Fig. 3). Due to significant sediment collapse over the last few decades and a lack of protection from the supporting cliff, the west sector is poorly understood.

The cultural sequence of Riparo Mochi was defined more than 50 years ago (Blanc et al., 1957–1961; Laplace, 1977) and is based on the typological classification of the lithic assemblages by Cardini and Laplace, as well as the observations of other scholars (Kuhn and Stiner, 1992, 1998; Palma di Cesnola, 1993; Kuhn and Bietti, 2000). Based on ongoing micromorphological and geoarchaeological analysis, the lowest part of the sequence, Unit I, is associated with Mousterian archaeological remains. Unit H is not a homogeneous

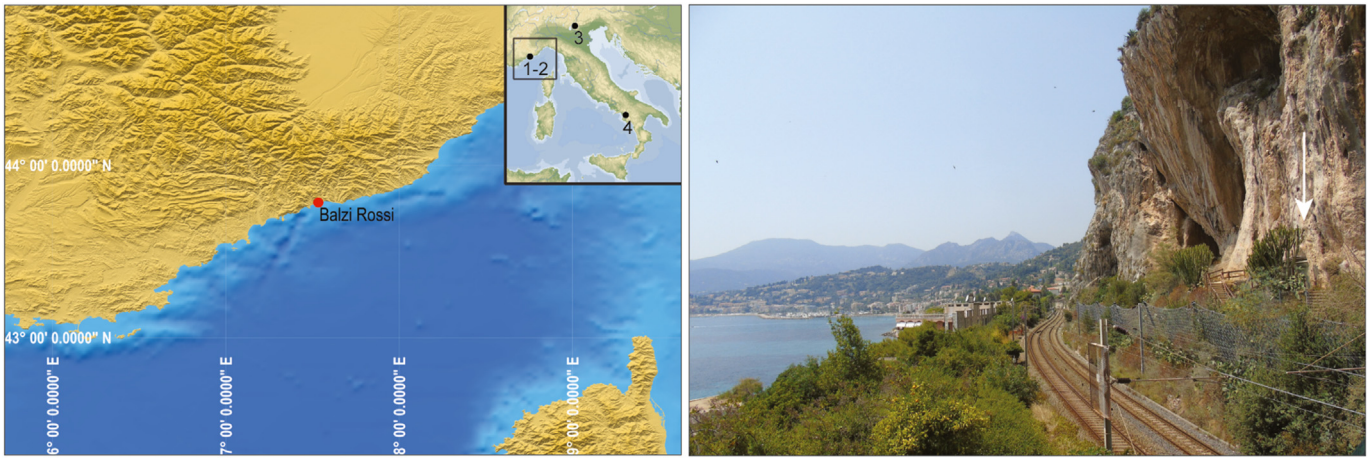

Figure 1. Location of the Balzi Rossi cliffs (left) and archaeological sites mentioned in this paper in the inset. 1: Riparo Mochi; 2: Riparo Bombrini; 3: Fumane; 4: Castelcivita. The Riparo Mochi site is indicated by an arrow (right). Photo: S. Grimaldi.

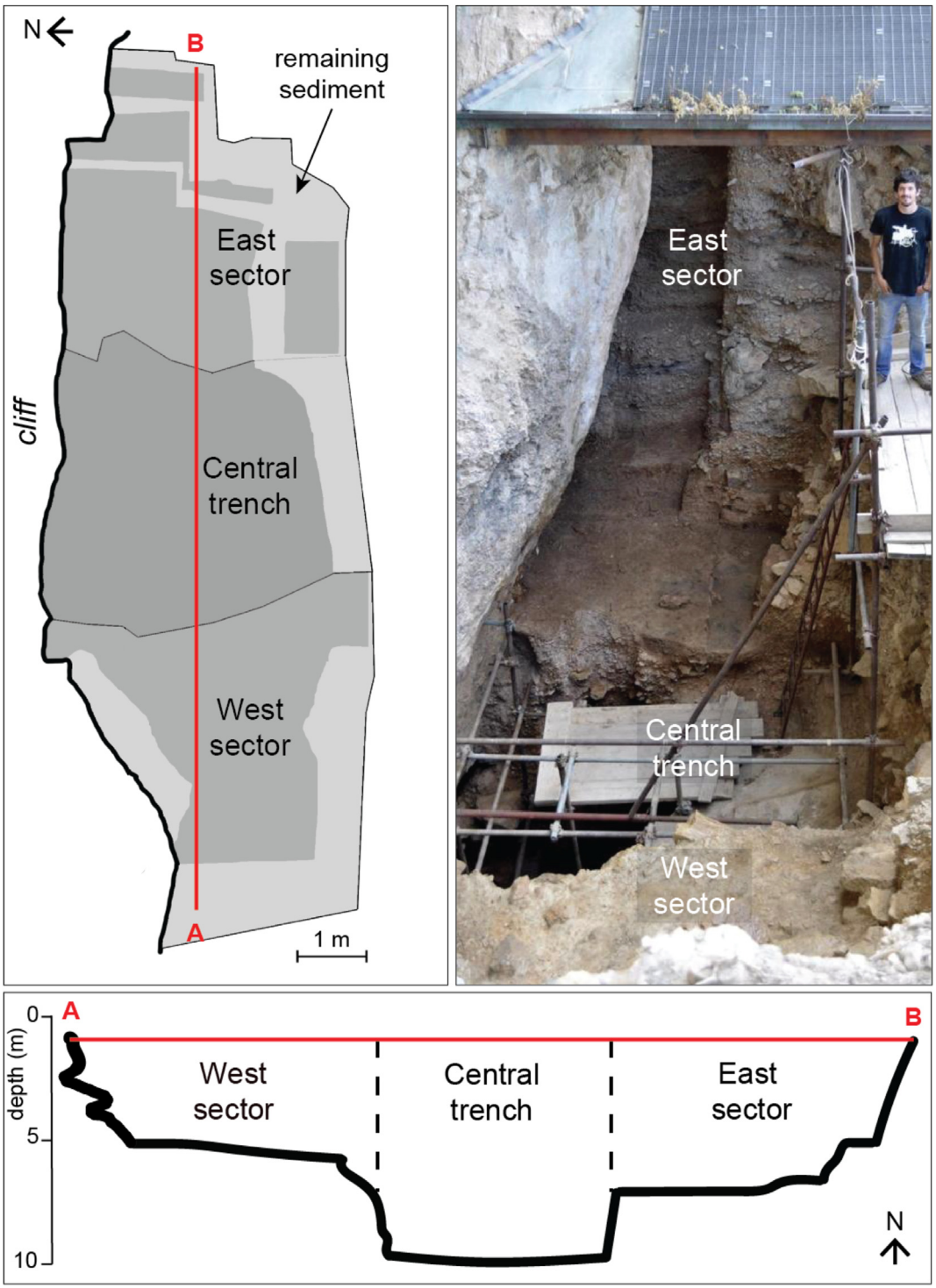

Figure 2. Plan of the excavation area (left) and longitudinal section of the excavated area (bottom). View of the rock shelter and the remaining deposit of the east sector and the central trench (right). Photo: S. Grimaldi.

lithological layer. Rather, it consists of about 40–50 cm of complexly interbedded lithological units that may be divided into three main layers (Grimaldi et al., 2014): 1) at the base, there is a scant but unmistakable presence of final MP evidence; today, this level should be referred to as the top of the Mousterian Unit I; 2) in the middle, there is a sterile layer about 10-cm thick; the thickness of this layer rapidly decreases toward the rock wall. From this point forward, this sterile layer should be referred to as Unit H; and 3) at the top, a 15 to 20-cm-thick sediment provides the earliest evidence of UP occupations at the site. This layer should be referred to as the base of Unit G. This cultural change divides the sequence into two main parts by a sharp and horizontal limit. Unit G is assigned to the Proto-Aurignacian (Laplace, 1977) or Early Aurignacian with Dufour bladelets (Bietti et al., 2004), and Unit F is a typical Early Aurignacian assemblage. Cardini's Unit E is very thin (10–20 cm, sometimes up to 25–30 cm) and is made up of reddish silty clay loam, with minor quantities of limestone skeleton. Some rare artifacts or faunal remains have been found. Unit D is defined

Table 1
Lithological description of macrounits with corresponding cultural assignations but whose chronostratigraphic position and limits were inferred a posteriori based on the characteristics of the embedded cultural remains.

Macrounit	Cultural assignation	Description
A	Epigravettian	~60 cm of breccia with frost shattered products embedded within a yellowish-brown sandy matrix.
B	Semisterile	~60 cm of colluvium.
C	Gravettian	~55 cm of frost shattered breccia within a yellowish sandy matrix. A thin red soil is present in the upper parts (possibly developed during an interstadial).
D	Noaillian Gravettian	~1.65 m of frost shattered breccia within a yellowish sandy matrix.
E	Semi-sterile	~20 cm of yellowish-brown sandy layer with scarce presence of frost shattered breccia.
F	Early Aurignacian	~1 m of frost shattered breccia within a yellowish sandy matrix.
G	Proto-Aurignacian	~50 cm of frost shattered breccia within a sandy matrix. Hearths were discovered at the base of this layer and hence the common occurrence of charcoal remains.
H	Earliest Upper Palaeolithic Proto-Aurignacian	~60 cm thick layer containing blocks and frost shattered breccia within a sandy matrix. Presence of some concretions.
I	Mousterian	~4.30 m thick layer. The upper part of the layer contains angular breccia interspersed within a sandy clay matrix.

as Gravettian with Noailles burins. Unit C is a Final Gravettian without Noailles burins. Unit B contains only a very few artifacts (similar to Unit E), and Unit A has been described as Epigravettian with geometrics (Pala di Cesnola, 1993).

Technofunctional studies of the lithic material have been undertaken more recently (Grimaldi and Santaniello, 2014; Grimaldi et al., 2014). These raw material studies reveal that the Mousterian assemblage is made of different rocks originating from outcrops at no more than 30 km away from the site (Grimaldi et al., 2014). These types of rocks have been exploited using the same production system, although differences in technical procedures have been observed in the Mousterian sequence. In fact, a regular main pattern occurs in the use of raw material. The core is firstly used to produce elongated products by means of a unidirectional sequence; later, it is exploited to produce shorter products. This secondary production stage implies different technical choices, such as the production of centripetal flakes (final Mousterian levels), debordant flakes, or irregular elongated flakes (earlier Mousterian levels). Nevertheless, some variability has also been identified in the increasing use/retouch of the different raw materials. From the bottom to the top of the sequence, the proportion of local to strictly local raw material remains similar throughout the sequence. In contrast, the Proto-Aurignacian assemblage reveals the presence of several repeated occupations characterized by laminar and flake production adapted to different types of raw material originating from the entire Liguro-Provencal Arc, over distances greater than 150–200 km (Grimaldi et al., 2014).

The site has yielded a rich faunal assemblage, and the vertebrate remains have been only partially studied for the last twenty years; currently, an exhaustive zooarchaeological research project is ongoing. In Unit I, the assemblage is dominated by ungulates (mainly red deer, wild boar, horse, and ibex; Alhaique, 2000), but carnivores, including bear, lion, panther, wolf, and hyena, are also present. Mammoth and elk remains are found in the lower section, whereas fallow deer were recovered in the upper section of Unit I (Arellano, 2009); this indicates a shift from colder to milder and more temperate climatic conditions toward the top of the Mousterian section. The UP Units G to C are mostly characterized by the presence of cervids and caprines and molluscan remains, typical of temperate climatic conditions (Tagliacozzo et al., 2012).

The 1949 and 1959 excavations also yielded abundant shell remains, around 6000 specimens (Stiner, 1999). The malacological collection was only partially classified and subdivided into four groups: ornamental, food refuse, an accidental by-product of sponge collection, and terrestrial snails coinhabiting the site. An exhaustive study of the entire malacological collection is ongoing.

1.2. Previous chronology

The published chronology for the site consists of 23 radiocarbon ages. The first five absolute ages from the site were produced in the early 1990s from charcoal samples collected from the Aurignacian Unit G during the 1959 excavations. These samples were dated at the Oxford Radiocarbon Accelerator Unit using accelerator mass spectrometry along with a routine acid-base-acid (ABA) pretreatment (Table 2; Hedges et al., 1994). Two samples of charcoal were also dated using ABA in the early 2000s (Douka et al., 2012; Bietti et al., 2004).

Douka et al. (2012) presented 16 radiocarbon ages on marine shell, mostly beads, and ABOx-SC-treated charcoal. Several studies (Bird et al., 1999; Higham et al., 2009; Douka et al., 2010a, b; Wood et al., 2012) have shown that the ABA method for cleaning Pleistocene-age charcoal often produces underestimates of the true age of the material, whereas ABOx-SC, a more aggressive and rigorous protocol, produces more reliable and reproducible results. The radiocarbon results from Douka et al. (2012) are shown in Table 2. The shell ages exhibited good agreement with most ABA- and the ABOx-treated charcoal, and the authors calculated a probability distribution for the start of the Proto-Aurignacian at the site (at ~37 ka BP or 42.7–41.6 ka cal BP, 68%). They noted, however, that the lack of data from the lower parts of the sequence meant that the start boundary length was likely to change with the addition of further ages from the lowermost Mousterian unit.

2. Material and methods

We used two dating methods in the current study: radiocarbon and luminescence, as described in the following subsections.

2.1. Radiocarbon dating

Ten new samples from different excavation or collection seasons (1959, 1997, and 2012–2013) were dated using radiocarbon. Three were limpet shells (*Patella* sp.), and seven were unidentified charcoal collected from the site's surviving East profile. Two shells (OxA-30629 and OxA-35352) were sampled directly from the existing East Sector section, in the vicinity of what is thought to be the basal hearth of Proto-Aurignacian unit G, and the hearth discovered in 1997 in unit H. All radiocarbon ages were produced at the Oxford Radiocarbon Accelerator Unit and are given an OxA-lab code.

The shell samples were dated using routine pretreatment procedures (Brock et al., 2010; Douka et al., 2010b), without using a

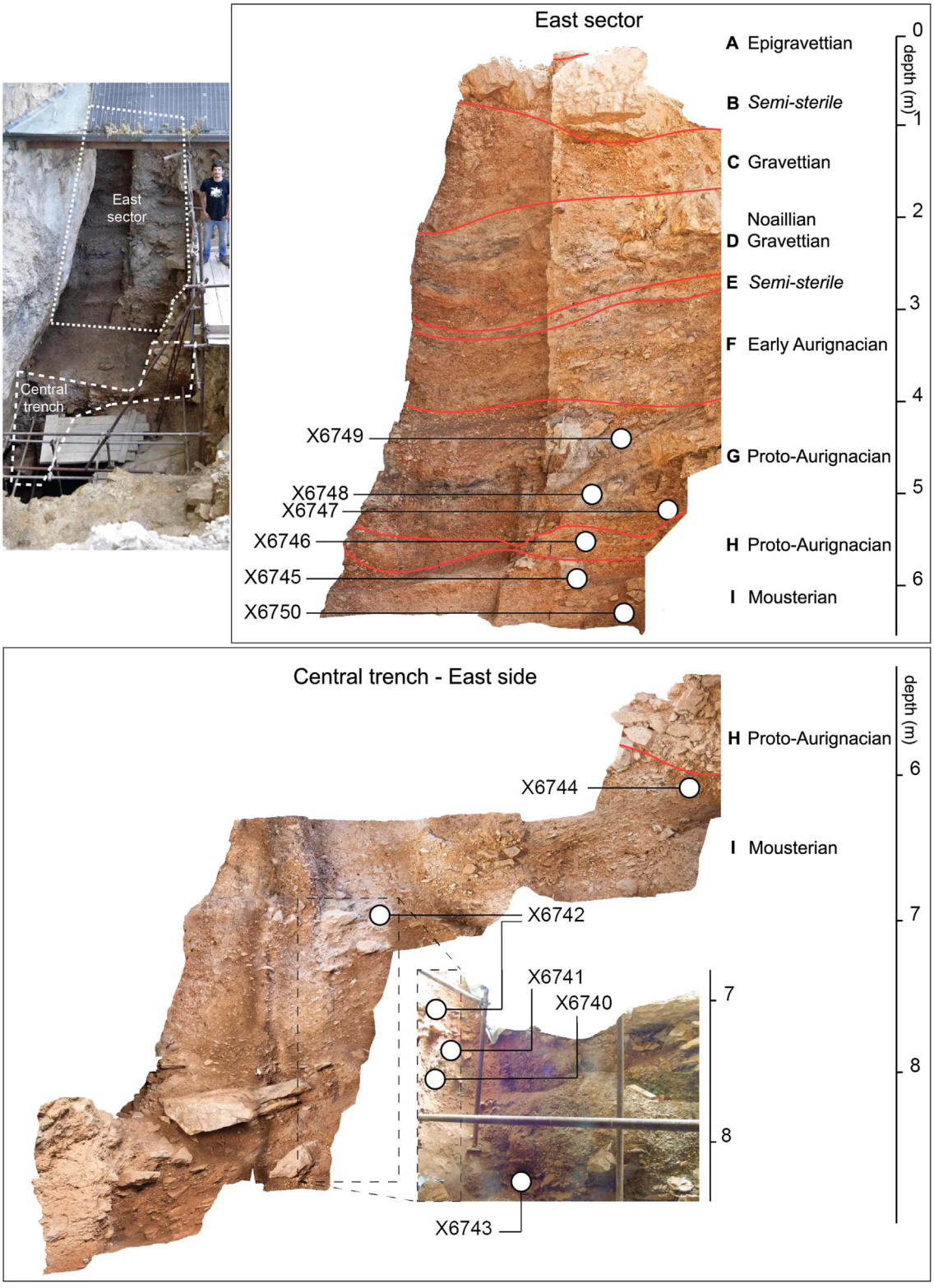

Figure 3. Stratigraphic position of the collected sediment samples for luminescence dating in the east sector (top right) and the central trench, east side (bottom). The red lines indicate the stratigraphic boundary between each macrounit. Unit A is not visible in these sections. Photo: S. Grimaldi. (For interpretation of the references to color in this figure legend, the reader is referred to the Web version of this article).

diagenesis screening test (due to their calcitic nature), and the charcoal samples were dated using ABOx-SC. Of the seven charcoals, three failed to produce enough carbon for accelerator mass spectrometry dating.

The radiocarbon ages were calibrated using IntCal20 (Reimer et al., 2020) and Marine20 (Heaton et al., 2020). The shell determinations were additionally corrected for the local Mediterranean reservoir effect ($\Delta R = 58 \pm 85$ ^{14}C years; Reimer and McCormac, 2002).

Table 2
Previously available radiocarbon dates from Riparo Mochi produced either in the Oxford (AMS) or in the Rome (conventional) laboratories.

Lab code	Level-cut	Material	^{14}C date	±	Reference
Excavation Cardini 1959					
Rome-1	F top (hearth)	Charcoal ABA	27230	570	Bietti et al. (2004)
OxA-3588	G 50	Charcoal ABA	32280	580	Hedges et al. (1994)
OxA-3589	G 51	Charcoal ABA	33400	750	Hedges et al. (1994)
OxA-3590	G 56-57	Charcoal ABA	34680	760	Hedges et al. (1994)
OxA-3591	G 59	Charcoal ABA	35700	850	Hedges et al. (1994)
OxA-3592	G 60	Charcoal ABA	34870	800	Hedges et al. (1994)
OxA-19569	G 60	Charcoal ABOx-SC	36350	260	Douka et al. (2012)
Rome-2	G base (hearth)	Charcoal ABA	37400	1300	Bietti et al. (2004)
Excavations Cardini 1959					
OxA-19800	D 29	*Cyclope neritea*	24600	100	Douka et al. (2012)
OxA-19801	E 32	*Cyclope neritea*	25490	110	Douka et al. (2012)
OxA-19857	F 34	*Cyclope neritea*	26030	110	Douka et al. (2012)
OxA-19728	F 40	*Cyclope neritea*	26410	110	Douka et al. (2012)
OxA-20629	F 44	*Mytilus* cf. *galloprovincialis*	32910	220	Douka et al. (2012)
OxA-19614	F 49	*Homalopoma sanguineum*	32370	160	Douka et al. (2012)
OxA-20360	G 51	*Mytilus* cf. *galloprovincialis*	31960	150	Douka et al. (2012)
OxA-19802	G 51	*Homalopoma sanguineum*	30770	150	Douka et al. (2012)
OxA-20630	G 54	*Homalopoma sanguineum*	33180	230	Douka et al. (2012)
OxA-19290	G 57	*Nassarius gibbosulus*	36750	210	Douka et al. (2012)
Excavations Bietti 1997–2003					
OxA-19729[a]	H 2	*Cyclope neritea*	26140	110	Douka et al. (2012)
OxA-22268[a]	HH 1	*Cyclope neritea*	24870	120	Douka et al. (2012)
OxA-19289[a]	I 3	*Cerastoderma glaucum*	32330	150	Douka et al. (2012)
OxA-19730[a]	I 5	*Trochus* sp.	34930	200	Douka et al. (2012)
OxA-20000[a]	I 5	*Trochus* sp.	36320	270	Douka et al. (2012)

The charcoals were treated with the ABA (acid-base-acid) protocol, with the exception of OxA-19569. This is an ABOx-SC redate of OxA-3592 a charcoal previously dated using the routine ABA pretreatment method (refer to the study by Douka et al., 2012 for details)
[a] Results not included in the final Bayesian models.

2.2. Luminescence dating: sampling and procedure

Luminescence dating is a major chronometric tool for late Quaternary studies; it is used to determine the age of sedimentary deposits (i.e., time of deposition) that were exposed to daylight before burial. Luminescence dating relies on the capacity of certain minerals to record the amount of natural radiation they have absorbed (dose) during burial (Aitken, 1998). In the laboratory, the energy stored in the mineral is measured in terms of a laboratory dose, equivalent in luminescence effect to the natural dose, and referred to as the equivalent dose (D_e, Gy). The rate of absorption of energy (dose rate, Gy/year) is derived from the knowledge of the natural (internal and external) radioactivity to which the mineral has been exposed. The quotient of these two values (equivalent dose/dose rate) yields the burial time. Generally, the preferred mineral is quartz due to its capacity to reset (bleach) in a few seconds (Godfrey-Smith et al., 1988). In comparison, K-feldspars bleach more slowly than quartz (Godfrey-Smith et al., 1988), leading to potential age overestimation if bleaching was insufficient. Furthermore, the luminescence signal in K-feldspar can be affected by anomalous fading—loss of luminescence signal with time—resulting in age underestimation if not corrected for or avoided. Many studies have demonstrated the importance of comparing results from these two minerals and their different signals to evaluate the accuracy of the final ages better (e.g., Buylaert et al., 2007; Gliganic et al., 2012; Murray et al., 2012; Guérin et al., 2012a; Duller et al., 2015; Frouin et al., 2017; Klasen et al., 2017). In the present study, both quartz and coarse feldspar grains were investigated.

Eleven sediment samples were collected in 2015 in the central trench and the east sector of the site, from the bottom to the top of the sequence: seven samples were collected from Unit I, one sample was collected from Unit H, and three samples from Unit G (see Fig. 3). The cemented nature of the sediments and the presence of large limestone blocks did not allow the insertion of opaque tubes. Instead, the sediment samples were collected during the day under an artificial shelter (with an opaque plastic tarpaulin sheet to protect from external daylight) and using red-orange LED lighting (~590 nm). Samples were taken by first cleaning and removing the exposed section and manually collecting the unexposed sediment in opaque plastic bags. For each sample, the total dose rate was determined by a combination of in situ radioactivity measurements and laboratory-based analyses of subsamples of the sediment.

Sediment samples were prepared under controlled low-level yellow light in a conventional manner to extract quartz and K-feldspar grains suitable for luminescence dating; these were prepared according to standard procedures (e.g., Wintle, 1997). After wet sieving, the coarse size fraction (180–225 μm or 125–225 μm) of each sample was treated with HCl (10%) and H_2O_2 (30%) to remove carbonates and fine organic matter, respectively. Quartz (density [ρ] between 2.58 and 2.70 g cm^{-3}) and K-feldspar ($\rho < 2.58$ g cm^{-3}) fractions were then separated using heavy liquid (sodium polytungstate). An additional hydrofluoric acid (HF) treatment (40% for 60 min), followed by an HCl rinse, was used to remove the outer alpha-irradiated layer of the quartz grains and to eliminate potential feldspar contamination. No HF was used on the feldspar-rich fraction. After rinsing, drying, and sieving, the quartz and K-feldspar fractions were mounted in stainless-steel cups using silicone oil, as aliquots ~4 mm in diameter (each containing a few hundred grains). Luminescence measurements were carried out using a Freiberg Instruments lexsyg research device (Richter et al., 2013) equipped with a ^{90}Sr/^{90}Y ring-shaped irradiation source (Richter et al., 2012) delivering 0.063 ± 0.002 Gy s^{-1} at the sample position (calibrated using Risø calibration quartz batch 98). The quartz OSL signal was stimulated with blue LEDs emitting at 470 ± 30 nm covered by a long-pass filter (3-mm Schott GG420). The resulting signal was detected by a PMT (Hamamatsu H7360-02) through an optical filter (7.7-mm Hoya U-340; transmission between ~290 and 370 nm). The feldspars were stimulated with near-infrared LEDs emitting at 850 ± 30 nm, and the luminescence

signal was detected through a combination of 3 mm of Schott BG 39 and 3.5 mm of AHF BrightLine HC 414/46 nm, giving a detection window centered on 410 nm. All measurements were performed in a nitrogen atmosphere.

A standard multigrain single-aliquot regenerative (SAR) measurement protocol (Murray and Wintle, 2000, 2003; Wintle and Murray, 2006) was used for quartz dose determination (see Supplementary Online Material [SOM] Table S1). The SAR procedure involves measuring the natural OSL and regenerative signals induced by four given doses, each measured for 40 seconds at 125 °C. After each natural and regenerative dose, a fixed test dose (~10 Gy) is given to correct the OSL signal for any sensitivity changes during the measurement sequence. A duplicate regenerative dose was included in the procedure to check the adequacy of the sensitivity correction, and the recuperation was measured after a zero-dose regenerative cycle. A stimulation at 280 °C held for 40 seconds was applied between each successive SAR cycle to fully reset the OSL signal. The infrared depletion ratio (Duller, 2003) was also measured on each aliquot to check for possible contamination by feldspar grains.

The fast component dominates the OSL signal from the Riparo Mochi samples (see LM-OSL measurements in SOM Fig. S1). The net intensity of the OSL signal was integrated over the first 0.8 seconds after subtracting an early background signal derived from the next 0.8 seconds of stimulation (from 0.98 to 1.6 seconds). To determine the preheat conditions for OSL measurement, preheat plateau and dose recovery tests were performed on two samples (details are provided in SOM Figs. S2 and S3). For all samples, the preheat was fixed at 240 °C for 10 seconds and the cut heat before the test dose was fixed at 200 °C. The overall average dose recovery ratio was 1.00 ± 0.03 ($n = 12$).

Between 16 and 27 aliquots were measured for each sample to obtain an equivalent dose (D_e) distribution. The D_e and their uncertainties were estimated by interpolating the sensitivity-corrected natural OSL signal onto the sensitivity-corrected regenerated growth curve, fitted using a single exponential function with the Analyst software v. 4.57 (Duller, 2018). For all samples, the D_e values are below the sample saturation limit (Murray and Wintle, 2003), suggesting that a reliable D_e can be estimated for all the samples (see SOM Fig. S4). The D_e distributions are reported for all samples in SOM Figure S5.

First, we calculated the unweighted mean of the D_e's (Table 5). The weighted mean was also determined from the Central Age Model, also referred to as the Central Dose Model (CDM) by Galbraith et al. (1999) using the function calc_CentralDose() (Burow, 2020) from the package Luminescence v. 0.9.11 (Kreutzer et al., 2012, 2020) in R v. 4.0.2 (R Core Team, 2020). The CDM is intended to be applied to samples composed of a single population of grains, i.e., well bleached before deposition, exposed to the same environmental dose rate during burial, and having remained unaffected by any postdepositional sedimentary processes. However, recent criticisms have suggested some issues regarding the CDM calculation and its uncertainty estimates (Combès et al., 2015), leading to potential age underestimates (Guérin et al., 2017), particularly for older samples (Heydari and Guérin, 2018). The Average Dose Model (ADM) proposed recently by Guérin et al. (2017) appears as an interesting alternative, as it is believed to provide a more satisfactory estimate of the average dose, mainly when grains have absorbed variable doses (Heydari and Guérin, 2018). Data analysis was carried out using the function calc_AverageDose() (Guérin et al., 2017). An intrinsic dispersion value (sigma_m) of 10% was used, which is higher than the average overdispersion (OD) obtained from the dose recovery tests performed on samples X6741 and X6747. Still, it accounts for any unrecognized measurement uncertainty.

K-feldspar dose values were determined using the elevated temperature post-infrared-infrared stimulated luminescence (pIRIR) protocol measured at 290 °C (Thiel et al., 2011; hereafter $pIRIR_{290}$; SOM Table S1). Standard SAR measurement protocols were applied using four regenerative doses and a zero-dose cycle. No corrections were made either for the residual or for the anomalous fading, as suggested by several authors (e.g., Thomsen et al., 2008; Jain and Ankjaergaard, 2011; Buylaert et al., 2012). The luminescence signals were obtained by integrating the first 2.5 seconds of the signal, and the background determined on the last 50 seconds was subtracted. The growth curve was fitted with a single saturating exponential function (see SOM Fig. S6) with Analyst v. 4.57 (Duller, 2018). The criteria for validating the application of the SAR protocol rely on the recycling ratio and the recuperation ratio, which have been met for all measured aliquots. The uncertainties on individual D_e values have been determined using conventional error propagation. The standard deviation takes into account the contributions from counting statistics and the curve fitting error. The D_e distributions are reported for all samples in SOM Fig. S7. The OSL and $pIRIR_{290}$ ages have been calculated using the online calculator DRAC v. 1.2 developed by Durcan et al. (2015).

2.3. Laboratory and field dosimetry

The total dose rate to sand-sized grains of quartz and feldspar comprises external contributions from beta, gamma, and cosmic radiation, plus an internal dose rate due to radioactive inclusions. An internal dose rate of 0.02 ± 0.01 $Gy.ka^{-1}$ was conservatively assumed for the quartz fraction. For K-feldspars, the K and Rb content was assumed to be 12.5 ± 0.5% and 400 ± 100 ppm, respectively, as suggested by Huntley and Baril (1997) and Huntley and Hancock (2001).

Beta dose rates were calculated from the U, Th, and K contents measured by inductively coupled (ICP) mass spectrometry and inductively coupled atomic emission spectroscopy, respectively, on a subsample of homogenized sediment (~8 g). Allowance was made for beta-dose attenuation due to grain size (Guérin et al., 2012b). The gamma component of the total dose rate was determined from the measurement of the luminescence signal recorded by dosimeters placed into the exposed section (5–20 cm from the sample location) for a duration of 642 days. These dosimeters consisted of three carbon-doped alumina pellets (Al_2O_3:C, diameter = 5 mm, thickness = 1 mm) placed at the extremity of an aluminum metal tube measuring ~30 cm in length (see details in the study by Kreutzer et al., 2019). Before burial, the pellets were heated to 350 °C to reset any remaining luminescence signal. Measurements were done at the IRAMAT-CRP2A laboratory using a Daybreak 2200 OSL reader system (Bortolot, 2000), combining green light LED stimulation (Nichia NSPG310) and 7.5 mm of Hoya U-340 filter for detection. The measured OSL signal from each pellet was compared to that induced by an artificial beta source (Mercier et al., 1994; Kreutzer et al., 2019). The dosimeters near samples X6747, X6742, X6741, and X6740 were not recovered, and the gamma dose rates for these samples were estimated from their U, Th, and K concentrations.

The cosmic-ray dose rates were estimated from the equations provided by Prescott and Hutton (1994), taking into account the burial depth of each sample, the sediment density, and the configuration and location of the site (shielding, altitude, latitude).

2.4. Bayesian modeling

To place both sets of results (radiocarbon and luminescence) within the same statistical framework, we built two Bayesian models using the OxCal platform v. 4.4.2 (Bronk Ramsey, 2009a; see

code in SOM S1). These models incorporate stratigraphic information for the dated samples and contexts along with the radiocarbon and luminescence likelihoods, mainly following the model framework and priors outlined in the study by Douka et al. (2012). Before modeling, systematic uncertainties between luminescence estimates were removed (see Table 5). Using a simulation method based on Markov Chain Monte Carlo, OxCal successively samples the solution to Bayes' theorem and produces a new series of probability distributions ('posterior' distributions) that include relative 'prior' archaeological information. An improved chronological framework can then be built to determine the degree of agreement between the dates and the sequence and obtain probability distribution functions (PDFs) for the boundaries (undated events) representing the transition between successive phases. These modeled boundary estimates are often of crucial importance in understanding transitions, beginnings, and ends of archaeological phases. We assessed the robustness of the model and the probability of individual likelihoods being outliers within each structured model using outlier detection methods and convergence values (Bronk Ramsey, 2009b). We used a t-type general outlier model with a prior probability set at 0.10 for the oldest radiocarbon estimates (Hedges et al., 1994; Bietti et al., 2004) and at 0.05 for the age determinations obtained more recently (Douka et al., 2012), as well as for all luminescence age estimates. For sample X6746, we included the dose rate–corrected ages with a prior probability set as 0.15.

3. Results

3.1. Radiocarbon dating

The four charcoal determinations ranged from 43 to 35 ka BP (=thousands of uncalibrated ^{14}C years before AD1950; Table 3). The three determinations from the Mousterian unit agree well with their stratigraphic position, whereas OxA-2579-40 from unit H, which is intermediate between Late Mousterian I and Proto-Aurignacian G, appears much younger. As suspected from previous work, in this study, Unit H also provides anomalous results for radiocarbon ages. It is possible that the material in this unit has been affected by postdepositional diagenesis and mixing (see Discussion).

In Unit G, two shells gave very similar ages at 34,830–33,900 cal BP at 95.4% probability (OxA-30629) and 34,660–33,870 cal BP at 95.4% probability (OxA-35352). These determinations are several millennia too young compared to previous charcoal and shell determinations (Table 2). The combination of the eleven previous radiocarbon determinations gives an age range of 39,520–39,076 cal BP (95.4% probability, using R_Combine() in OxCal) for Unit G. The reasons for this discrepancy are unknown, but given that the largest degree of variation in current and previous dating studies of Mochi affect shell samples, we must consider the possibility of diagenetic alteration of the shell matrix. In most cases, the dated shells are limpets (*Patella* sp.). These species are among the few gastropods that originally secrete calcite and not aragonite to produce their shell exoskeleton. Calcite, however, is also the end product of secondary diagenesis, i.e., it is the mineral that forms postdepositionally when dissolution and recrystallization of the original shell matrix take place. These processes can affect the radiocarbon age of a molluscan shell, particularly if the system is an 'open' one with the input of recrystallized bicarbonate of a different age to the shell (Douka, 2017). A third shell sample found in cut 13 of the 1959 excavations (equivalent to the top of unit D) gave an age of 420–570 AD (95.4% probability) and is presumed to be a recent intrusion.

3.2. Dosimetry

Mochi is a stone-rich environment, and sediment samples were taken primarily to estimate the beta dose rate, which is derived mainly from the matrix between the calcareous lumps. This matrix was the material preferentially sampled for ICP analyses. Radioelement concentrations are reported in SOM Table S2. Because these large clasts will be lower in radioactive concentrations than the finer matrix, the gamma dose rates could be overestimated for the samples with no dosimeters. Nevertheless, both methods of gamma dose rate estimation give indistinguishable values, except for sample X6746 (see SOM Fig. S8), for which the in situ measured gamma dose overestimates the ICP result by 30%. On the remaining portion of each sample (except for X6746 due to lack of material), U-series disequilibria were tested using a high-resolution low-background gamma spectrometer housed at the Risø Laboratory, Denmark. Because the ^{238}U activities were not precisely measured, the ^{226}Ra/^{238}U ratio in some samples is poorly known (SOM Table S3). Nevertheless, the weighted average is 0.96 ± 0.06 (n = 10, mean ± se), and we concluded that there is no evidence for significant disequilibrium in these samples. We assume such a ratio did not change over time, and in situ measurements of the gamma dose rate contribution were used to calculate the total dose rate when possible.

For samples from Riparo Mochi, the water content at sampling (July 2015) was determined to be ~7%, on average. The measurement of water saturation content yielded an average value of ~27%. We assumed a past moisture content of 11 ± 5% (at 1 σ) for the age calculations, which allows for extreme past fluctuations of moisture, from 1 to 21% (at 2 σ). The total dose rates based on geochemistry, gamma, and cosmic contribution and estimated water content history were calculated following Aitken (1990) and the conversion factors of Guérin et al. (2011), using the dose rate

Table 3
New radiocarbon determinations from shell and charcoal samples from Riparo Mochi.

OxA	P code	Pretreatment	Year of excavation	Unit/cut (tg)	Cultural assignation	Material	Species	^{14}C Date (yr BP)	±
31486[a]	36582	Acid hydrolysis	1959	Tg 13, East sector		Shell	*Patella* sp.	1580	40
30629[a]	36635	Acid hydrolysis	Section 2013	G hearth? from section	Proto-Aurignacian	Shell	*Patella* sp.	31920	190
35352[a]	36635	Acid hydrolysis	Section 2013	G hearth? from section	Proto-Aurignacian	Shell	*Patella* sp.	31870	160
X-2579-40	36631	ABOx-SC	1997	H, A1 hearth, sample no.13 (rescue)	Proto-Aurignacian	Charcoal	not identified	35550	550
30736[a]	36581	Acid hydrolysis	1997	H hearth, sample no. 23 (rescue)	Proto-Aurignacian	Shell	*Patella* sp.	31580	200
X-2586-21	36632	ABOx-SC	2012	Top I, tg 10, sample no. 29	Very final Mousterian	Charcoal	Not identified	42100	2200
30201	36633	ABOx-SC	2012	Top I, tg 11, sample no. 30	Very final Mousterian	Charcoal	Not identified	42450	800
30187	36630	ABOx-SC	2012	Top I, tg 16, grey sediment	Final Mousterian	Charcoal	Not identified	43000	900
_	36634	ABOx-SC	1959	G tg 62		Charcoal	Failed due to low yield		
_	36637	ABOx-SC	2013	G base hearth, from section		Charcoal	Failed due to low yield		

[a] Results not included in the final Bayesian models.

Table 4
Environmental dose rate data for Riparo Mochi sediment samples.

Sample	Unit	Depth (m)	Grain size fraction (microns)	External dose rate[a] (Gy.ka^{-1})			Internal dose rate (Gy.ka^{-1})		Total dose rate[e] (Gy.ka^{-1})	
				Cosmic[b]	Gamma[c]	Beta	Quartz	F-feldspar[d]	Quartz	K-feldspar
X6749	G	4.2	125–250	0.12 ± 0.02	0.38 ± 0.02	0.68 ± 0.05	0.02 ± 0.01	0.64 ± 0.22	1.20 ± 0.06	1.95 ± 0.24
X6748	G	4.6	125–250	0.12 ± 0.02	0.34 ± 0.04	0.42 ± 0.03	0.02 ± 0.01	0.64 ± 0.22	0.90 ± 0.05	1.65 ± 0.24
X6747	G	5	125–250	0.12 ± 0.02	0.54 ± 0.06	0.81 ± 0.06	0.02 ± 0.01	0.64 ± 0.22	1.49 ± 0.09	2.24 ± 0.25
X6746	H	5.5	125–250	0.12 ± 0.02	0.42 ± 0.03	0.39 ± 0.03	0.02 ± 0.01	0.64 ± 0.22	0.94 ± 0.04	1.69 ± 0.24
X6750	I	5.9	180–250	0.12 ± 0.02	0.51 ± 0.04	0.85 ± 0.06	0.02 ± 0.01	0.72 ± 0.16	1.50 ± 0.07	2.36 ± 0.16
X6745	I	5.7	125–250	0.12 ± 0.02	0.47 ± 0.03	0.77 ± 0.05	0.02 ± 0.01	0.64 ± 0.22	1.38 ± 0.08	2.13 ± 0.25
X6744	I	6	180–250	0.10 ± 0.02	0.36 ± 0.03	0.61 ± 0.04	0.02 ± 0.01	0.72 ± 0.16	1.09 ± 0.06	1.95 ± 0.15
X6742	I	7.1	180–250	0.10 ± 0.02	0.47 ± 0.05	0.64 ± 0.04	0.02 ± 0.01	0.72 ± 0.16	1.22 ± 0.07	2.08 ± 0.15
X6741	I	7.3	180–250	0.10 ± 0.02	0.49 ± 0.05	0.71 ± 0.05	0.02 ± 0.01	0.72 ± 0.16	1.31 ± 0.07	2.17 ± 0.16
X6740	I	7.6	125–250	0.10 ± 0.02	0.40 ± 0.04	0.57 ± 0.04	0.02 ± 0.01	0.64 ± 0.22	1.09 ± 0.06	1.84 ± 0.24
X6743	I	8.7	180–250	0.10 ± 0.02	0.23 ± 0.02	0.38 ± 0.02	0.02 ± 0.01	0.72 ± 0.16	0.72 ± 0.04	1.58 ± 0.14

[a] External dose rates include adjustments for the water content.
[b] Cosmic-ray dose rates were estimated using the approach of Prescott and Hutton (1994) and assigned a relative uncertainty of ±20%.
[c] Gamma dose rates were determined from the dose recorded by in situ dosimeters except for samples X6747, X6742, X6741, and X6740, for which the gamma dose rates were calculated from the concentrations of potassium (K), uranium (U), and thorium (Th) within the sediment. We added a 5% error on these values.
[d] The internal feldspar dose rate is based on an internal ^{40}K concentration of 12.5 ± 0.5% and a Rb concentration of 400 ppm.
[e] Mean ± total uncertainty (1 sigma) calculated as the quadratic sum of the random and systematic uncertainties.

and age calculator DRAC v.1.2 developed by Durcan et al. (2015). Results of the different contributions to the dose rates are presented in Table 4.

3.3. Quartz measurements

To compare the D_e results obtained from three methods (Table 5), we first calculated the unweighted mean of the three methods for each sample and compared each method to that mean. The average of the unweighted means to mean ratio is 0.99 ± 0.05 (the error is given as the standard deviation), the CAM to mean ratio is 0.98 ± 0.05, and the ADM to mean ratio is 1.03 ± 0.10. The three models are all consistent with the mean at 2 sigma, and we cannot detect a difference in the analyses. The OD values are compatible for both CDM and ADM models ranging from 4 to 22%. The origin of such OD is challenging to determine on multigrain aliquots because of the averaging effects. From our dose recovery tests, the OD is expected to be around 5% for a single population of grains. Therefore, for most samples in this study, the additional scatter might be caused by microdosimetry variations, heterogeneous bleaching, and/or postdepositional mixing. Previous studies on the mineralogy of the Riparo Mochi sediments (Khatib et al., 2012) suggested that no quartz or other silicate minerals occur in the rock shelter limestone walls (SOM Fig. S9)—both quartz and felspar are allochthonous, mainly of aeolian origin. However, colluvial inputs have also been identified in some units as reddish pedorelics of terra rossa–like soils containing grains, as visible on the microphotograph of a sediment thin section in SOM Fig. S10. Therefore, it is possible that microdosimetry effects contribute to the large OD in the D_e's.

3.4. Feldspar measurements

The dose unweighted averages are reported in Table 5 with the weighted means calculated using the CDM and ADM models. The three models give statistically indistinguishable results. The OD values are less than 10%, except for sample X6747 which has an OD of 24%, reflected in the standard error on its D_e.

3.5. Luminescence age estimates

The age results are reported in Table 5 (see also SOM Figs. S11–S14). Optical stimulated luminescence quartz and $pIRIR_{290}$ feldspar ages generally increase with burial depth as expected. One noticeable exception is sample X6746, for which the quartz age appears much older than for the samples localized stratigraphically above and below. While the D_e of this sample is consistent with the stratigraphy, its dose rate is much lower than those above and below. We remarked in Section 3.2 that the in situ gamma dose overestimated the ICP-based result by 30%, which suggests that the beta dose rate we determined on a portion of this sediment is probably incorrect (perhaps due to an analytical problem or a lack of representativity of the sample used for the ICP analyses). If we calculate the average dose rates based on the samples located directly above and below this sample, the corrected quartz age becomes 48.7 ± 2.9 ka, and the corrected feldspar age 45.7 ± 5.0 ka, results which are much more consistent with the stratigraphy.

Quartz and feldspar ages are consistent at 2 sigma through the sequence. However, it is noticeable that in the lower part of the sequence (Fig. 4), the quartz ages are systematically older than the K-feldspar $pIRIR_{290}$ ages by ~10–30% (n = 6). Given the very different bleaching rates (perhaps by a factor of ~100; refer to the study by Murray et al., 2012) of the fast component in quartz and the $pIRIR_{290}$ signals in feldspar, this is strong evidence that the quartz signals were fully bleached at the time of deposition.

The absence of fading correction on the $pIRIR_{290}$ D_e's may explain the underestimation of the pIRIR results. If we consider a low hypothetical anomalous fading rate of 1.0 ± 0.5%/decade, the corrected pIRIR ages will appear older by 5% (see fading corrected ages in SOM Fig. S14). Wrong estimation of the feldspar internal dose rate could also explain this apparent age underestimation. Here we assumed that the signal was dominated by grains containing 12.5 ± 0.5% of potassium. Some recent studies suggest that a value of 10 ± 2% might be more appropriate in some cases (Smedley et al., 2015). The latter would give older ages by 8% (on average) and therefore would be more consistent with the quartz OSL results. However, the feldspar ages seem overall more coherent with the age determinations given by the independent dating method that is radiocarbon. Given all these aspects, it is extremely difficult to determine the most robust set of results.

3.6. Age-depth Bayesian modeling

Model 1 contains most radiocarbon determinations from the current and previous studies and all available luminescence

Table 5
Summary of the luminescence measurements and final age estimates of the Riparo Mochi samples.

Mineral	Sample Lab code	Unit	n[a]	unw. mean $D_e \pm se$ (Gy)	CDM $D_e \pm se$[b] (Gy)	OD[b] (%)	ADM $D_e \pm se$[c] (Gy)	Sigma_d[c] (%)	Age ± se [rd][d] (ka)
Quartz	X6749	G	24 (24)	53.45 ± 1.33	53.02 ± 1.22	3 ± 5	53.05 ± 1.28	3 ± 3	44.16 ± 2.30 [1.18]
	X6748	G	21 (22)	44.00 ± 1.23	43.05 ± 1.18	5 ± 5	43.59 ± 1.18	5 ± 3	48.54 ± 2.90 [1.38]
	X6747	G	14 (18)	69.47 ± 3.29	68.77 ± 2.99	12 ± 4	69.23 ± 2.96	11 ± 5	46.55 ± 2.31 [2.03]
	X6746	H	23 (26)	73.84 ± 2.79	72.81 ± 2.66	13 ± 3	73.44 ± 2.74	13 ± 3	78.15 ± 4.67
									49.14 ± 3.15 [1.99][e]
	X6750	I	25 (27)	75.36 ± 2.88	74.78 ± 2.69	14 ± 3	75.52 ± 2.90	14 ± 3	50.29 ± 3.07 [1.95]
	X6745	I	11 (16)	77.75 ± 3.12	77.11 ± 2.90	5 ± 6	77.23 ± 2.75	5 ± 4	56.03 ± 3.68 [2.08]
	X6744	I	25 (25)	72.31 ± 3.06	71.32 ± 2.65	15 ± 3	72.09 ± 2.92	15 ± 4	65.88 ± 4.30 [2.67]
	X6742	I	16 (16)	86.30 ± 5.99	83.40 ± 5.51	24 ± 5	85.74 ± 5.84	24 ± 3	70.09 ± 6.20 [4.71]
	X6741	I	14 (17)	73.76 ± 3.59	72.68 ± 3.28	13 ± 4	73.26 ± 3.44	13 ± 5	55.82 ± 4.05 [2.61]
	X6740	I	19 (19)	89.90 ± 5.79	85.72 ± 4.75	21 ± 4	87.65 ± 5.33	21 ± 3	80.34 ± 6.62 [4.88]
	X6743	I	15 (16)	67.74 ± 3.81	66.03 ± 3.26	15 ± 4	66.81 ± 3.38	15 ± 5	92.41 ± 6.87 [4.64]
Feldspar	X6749	G	10 (10)	85.01 ± 3.34	84.33 ± 3.14	5 ± 7	84.42 ± 3.10	5 ± 4	43.23 ± 5.60 [1.59]
	X6748	G	10 (10)	76.88 ± 2.81	76.12 ± 2.74	3 ± 10	76.15 ± 2.82	3 ± 3	46.18 ± 6.96 [1.70]
	X6747	G	10 (10)	104.20 ± 8.09	100.62 ± 8.53	24 ± 7	103.67 ± 8.17	24 ± 8	49.30 ± 6.34 [3.60]
	X6746	H	14 (14)	99.53 ± 3.34	98.61 ± 2.90	0	98.61 ± 2.91	0	58.34 ± 8.46
									42.86 ± 3.99 [1.40][e]
	X6750	I	13 (12)	126.84 ± 5.61	121.86 ± 4.98	10 ± 4	122.42 ± 5.78	10 ± 5	51.83 ± 4.20 [2.42]
	X6745	I	10 (10)	106.54 ± 2.55	106.09 ± 4.12	0	106.09 ± 2.49	0	49.80 ± 5.92 [1.21]
	X6744	I	9 (9)	106.04 ± 1.68	106.00 ± 4.27	0	106.00 ± 1.89	0	54.25 ± 4.25 [1.00]
	X6742	I	9 (9)	113.64 ± 4.30	112.68 ± 4.58	0	112.68 ± 4.55	2 ± 2	54.10 ± 4.57 [2.16]
	X6741	I	10 (10)	108.88 ± 3.78	107.25 ± 4.28	0	107.24 ± 3.78	0	49.37 ± 3.95 [1.72]
	X6740	I	10 (10)	109.11 ± 2.88	108.19 ± 4.21	0	108.19 ± 2.95	0	58.73 ± 7.93 [1.62]
	X6743	I	10 (10)	109.72 ± 5.16	107.69 ± 4.74	6 ± 7	107.91 ± 4.76	6 ± 5	68.23 ± 6.89 [2.96]

Abbreviations: unw. mean = unweighted mean; CDM = Central Dose Model; De = Equivalent dose; OD = overdispersion; ADM = Average Dose Model; se = standard error; rd = random error.

[a] Number of aliquots accepted (measured).

[b] De and OD values were calculated using the CDM (Galbraith et al., 1999), using the calc_CentralDose() function from the package Luminescence v. 0.9.11 (Kreutzer et al., 2020) in R v. 4.0.2 (R Core Team, 2020), with the parameters: sigmab = 0.10, log = TRUE.

[c] De and sigma_d values were calculated using the ADM (Guérin et al., 2017), using the calc_AverageDose() function from the package Luminescence v. 0.9.11 (Kreutzer et al., 2020) in R v. 4.0.2 (R Core Team, 2020), with the parameters: sigma_m = 0.10, log = TRUE.

[d] Age calculated using the dose rate and age calculator DRAC v. 1.2 (Durcan et al., 2015). Equivalent doses are from the ADM. The uncertainty shown after the ± symbol is the quadratic sum of the random and systematic uncertainties at 1 sigma; values shown in brackets are the random-only errors.

[e] Corrected dose rate used for the age determination.

determinations on quartz (Fig. 5). Model 2 includes the same radiocarbon determinations, but the luminescence determinations are this time on feldspar (Fig. 6). Of the thirty-three determinations included in model 1, four luminescence dates were identified as outliers (X6741, X6746, X6748, and X6749) and three radiocarbon determinations (OxA-X-2579-40, OxA-20360, and OxA-19802; see SOM Tables S4 and S5). From layer H, both determinations X6746 (corrected) and OxA-X-2579-40 are incompatible with each other, as well as the modeled ages of the units above and below. Once again, Unit H is a problematic part of the site and proves difficult to date directly (see Discussion). In model 2 (SOM Tables S6 and S7), only one luminescence date was identified as an outlier (X6741) and four radiocarbon determinations (OxA-X-2579-40, OxA-20630, OxA-20360, and OxA-19802). The radiocarbon determinations from higher up the sequence had been previously identified and discussed by Douka et al. (2012).

3.7. Comparing the models

To examine whether models 1 and 2 produced consistent age models, we calculated the difference between boundaries from one model to another, assuming that the PDFs of the boundaries approximate a normal distribution. The mean and standard deviation of each boundary within both models was estimated in OxCal in the 68.2% and 95.4% probability range. If the difference between PDFs of each boundary includes zero in the 68.2% or 95.4% probability range, then the PDFs are regarded as indistinguishable in the respective probability range. The total error is the standard deviation of each PDF added in quadrature. The results are given in Figure 7. The two models are consistent as all boundaries overlap at 68.2%.

4. Discussion

4.1. Chronostratigraphy

We base the following discussion on the results given by model 2, which yields an overall better consistency of the luminescence and radiocarbon age results (i.e., fewer outliers) and given at 2 sigma. These new results clarify the chronostratigraphic succession between the Middle to Upper Paleolithic occupation at the site. Most radiocarbon determinations were produced on samples coming from the UP units of Cardini's 1959 excavations at the eastern part of the site. In contrast, the luminescence ages cover both the earliest UP as well as the MP parts of the sequence.

The earliest currently available age for the Mousterian deposit at the site comes from mid Unit I and is dated from the MIS 5. The rest of the Mousterian deposit is dated by six luminescence determinations (X6740, X6741, X6742, X6744, X6745, and X6750) up to ~46 ka. One charcoal sample found in 2012 at the top of Unit I attributed to the latest Mousterian deposit (Unit I) gave an age estimate beyond the radiocarbon limit (OxA-X-2586-21), while two other charcoals were dated between 48 and 44 ka cal BP (OxA-30187, OxA-30201 at 2 sigma). These determinations allow us to place the Mousterian within MIS 4 and track its development in the early stages of MIS 3. The recently published micromammal assemblage (Berto et al., 2019) from Unit I suggests the presence of an environment characterized by small clumps of trees in an open rocky area with species associated with very cold conditions. The end of the Mousterian and the transition to unit H is placed between 45.8 and 41.9 ka (95.4% probability) according to our Bayesian model 2 (Fig. 6; SOM Table S7).

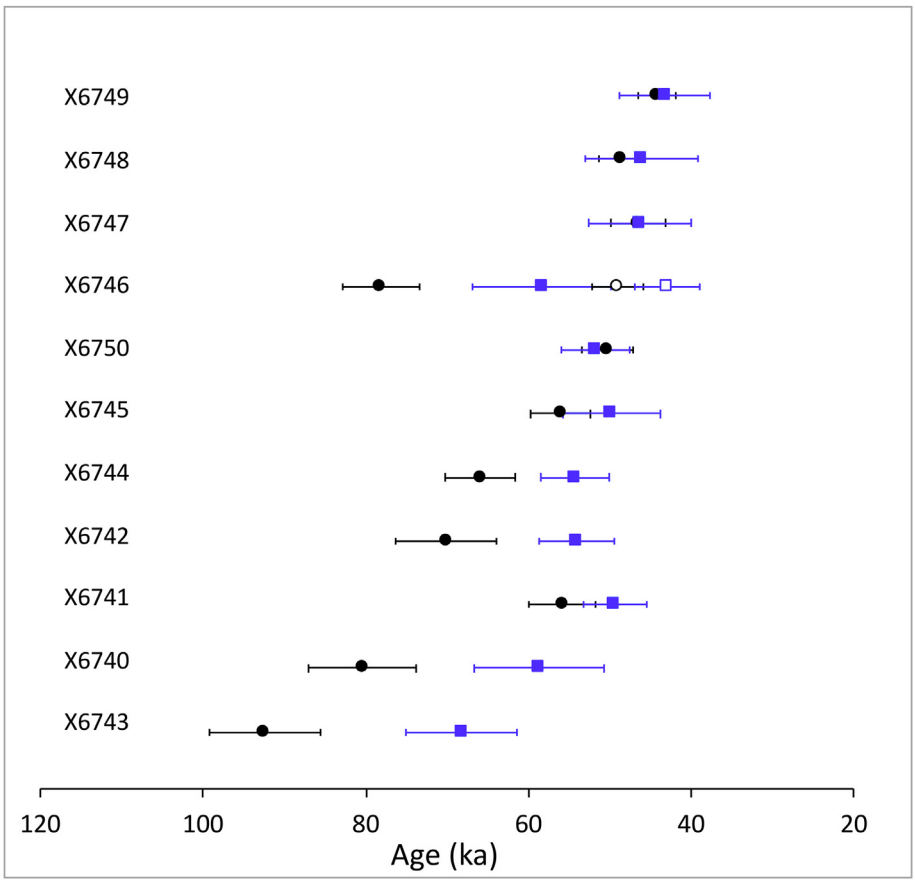

Figure 4. Quartz OSL (circle) and K-feldspar pIRIR$_{290}$ (square) age results (+/− 1 sigma) in stratigraphic order, using the Average Dose Model (see SOM Figs. S11–S14 for other models). Empty symbols indicate the dose rate corrected ages for sample X6746.

Cardini described Unit H as semisterile, with a mixture of Middle and Upper Paleolithic elements. In the more recent excavations, however, in situ features such as hearths were identified, and it is therefore possible that, instead of Unit G as previously thought, it is the upper part of Unit H that represents the earliest Proto-Aurignacian at the site as previously demonstrated by Grimaldi et al. (2014). However, sedimentary structures related to erosion and redeposition are also present within Unit H, mainly observed in the Sector East excavated by Cardini in 1959, suggesting that at least part of the MP–UP association may be affected by local processes of reworking. However, the small excavation area and the low number of artifacts from Unit H render this only a working hypothesis. One charcoal sample (OxA-X-2579-40) was dated at 41.3–39.0 ka cal BP (95.4% probability). This appears slightly too young compared to previous estimates obtained for the overlying Unit G. A luminescence sample from Unit H yielded a corrected age of 42.86 ± 3.99 ka. As previously discussed, Unit H comprises multiple lithologic units; some of these are combustion features that should be reasonably in situ, whereas others are scour-and-fill channels that indicate erosional phases followed by fast deposition of sediment reworked from older units. Given that the radiocarbon age determinations from Unit H were deemed to be outliers in the Bayesian models, OxCal produced posterior probability distributions in the form of boundaries that are constrained mainly by the ages of underlying and overlying deposits, i.e., Units I and G, respectively.

Unit G contains large hearths, thousands of lithic artifacts, shell and stone beads, and all the hallmarks of the Proto-Aurignacian. Dating the beginning of this formation can securely pinpoint an age estimate for this significant part of the occupation of the site. The previous age estimates for the start of Unit G were 42.7–41.6 or 44.0–41.8 ka cal BP (Douka et al., 2012; Fig. 7). The boundary for the end of Unit H and the start of Unit G is now placed at 44.3–41.1 ka (95.4% probability) according to our Bayesian model 2 (Fig. 6; SOM Table S7). As we move up the stratigraphic sequence, the radiocarbon and luminescence dates follow, as expected, a consistent decreasing pattern in age.

4.2. Regional context

Placing the new chronostratigraphic sequence from Mochi in its regional and broader context is important given that several northern Italian Paleolithic sites have been reanalyzed and redated in recent years (Fig. 8). Riparo Bombrini is part of the same archaeological complex as Mochi and has recently been reevaluated. The site was excavated in 1976 and again in the early 2000s. Higham et al. (2014) and Benazzi et al. (2015) presented a series of dates from the 1976 Vicino excavations. The 1976 sequence was divided into four artificial spits containing two cultural macrounits: the lower one (Upper and Lower level IV) with Mousterian artifacts and the upper one (levels III-I) containing UP artifacts. Levels III and II have yielded Proto-Aurignacian artifacts, abundant Dufour bladelets, beads, bone points, as well as a modern human tooth.

Based on a Bayesian model of the 14 determinations from Bombrini (Benazzi et al., 2015, their Fig. 3), the start of the Proto-Aurignacian is placed at 39.5–36.7 ka cal BP or 40.0–36.5 ka cal BP (68/95% probability), whereas the end of the Mousterian part of

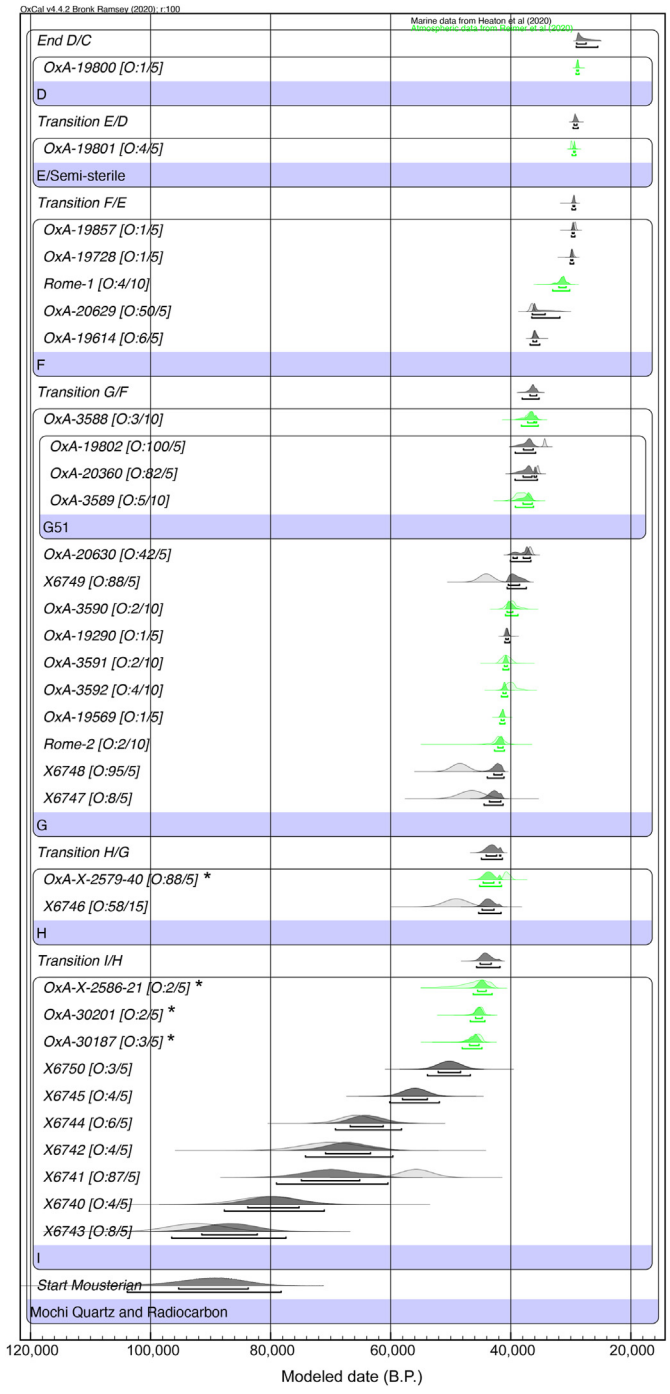

Figure 5. Model 1. Bayesian model of calibrated and modeled radiocarbon determinations from the current (asterisk) and previous studies with all available luminescence determinations on quartz. Outlier results are shown in [O: posterior outlier/prior outlier] format. CQL code and results are reported in SOM S1.

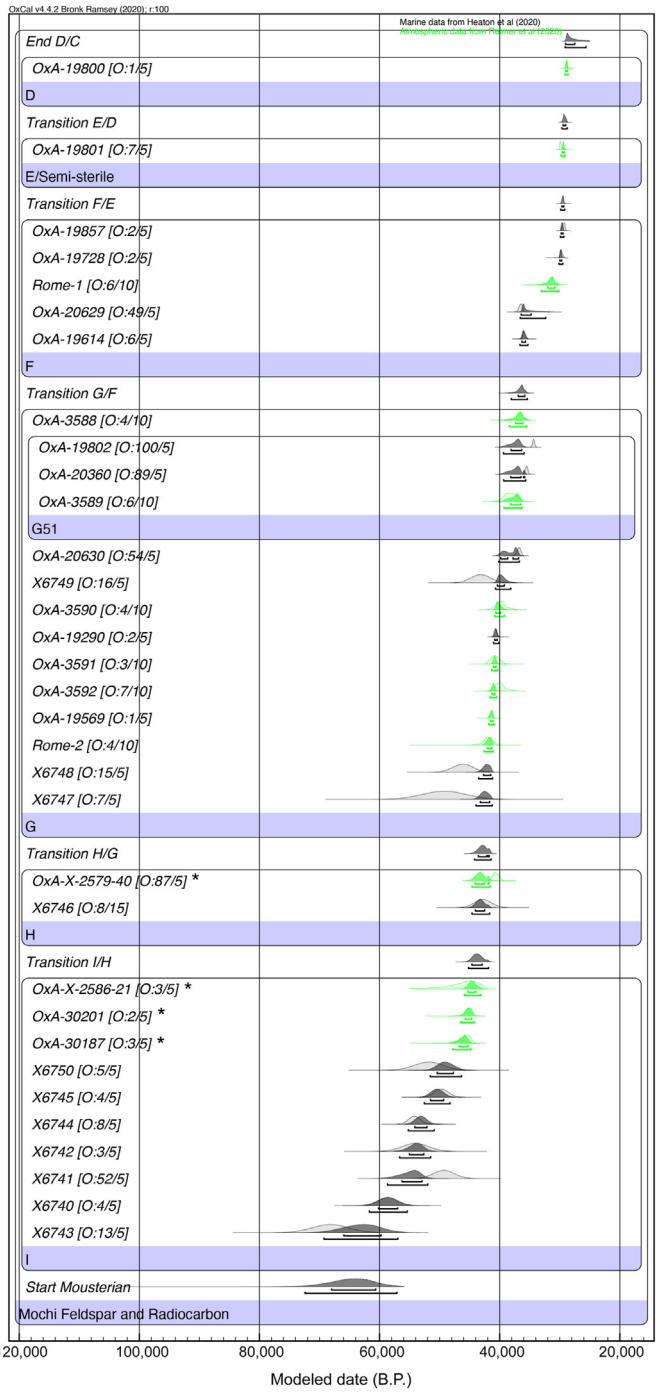

Figure 6. Model 2. Bayesian model of calibrated and modeled radiocarbon determinations from the current (asterisk) and previous studies with all available luminescence determinations on feldspar. Outlier results are shown in [O: posterior outlier/prior outlier] format. CQL code and results are reported in SOM S1.

the sequence falls between 40.9 and 39.6 ka cal BP or 41.1–38.6 ka cal BP (68/95% probability). Both estimates are a few millennia later than the respective start and end boundaries at Mochi. We note that the lower part of the Bombrini sequence is dated only by four shells, whereas the upper part contains dates made of bone and charcoal samples. Moreover, the two bone samples from the Proto-Aurignacian level LIII dated to 38.9–38.1 ka cal BP (95% probability; MAMS 21662) and 37.6–36.4 ka cal BP (95% probability; MAMS 21663), respectively, also present low amounts of extracted collagen (1.4 and 0.9% collagen respectively) and have high C:N ratios (3.5 and 3.4, respectively), both of which may indicate possible contamination. With uncertainties in the depositional history of the shells, the diagenetic potential of shell in general, and possible bone contamination, further dating at Bombrini is required for a proper comparison with the more complete and longer Mochi sequence, as the materials from these two sites are only about one hundred meters away and possibly suggesting the presence of a large living area linking the two sites.

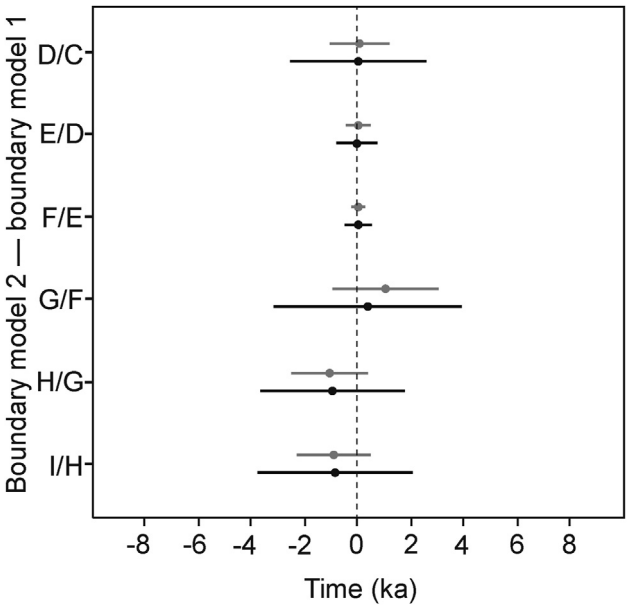

Figure 7. Difference between the probability distribution functions (PDFs) of the boundaries calculated in model 1 and model 2 at 68.2% probability (in gray) and 95.4% probability (in black). The bar represents the error calculated in quadrature.

At Bombrini, Benazzi et al. (2015:795) concluded that "the Proto-Aurignacian dispersal may therefore have been a cause (either directly or indirectly) of the extinction of the Neanderthals, at least in northern Italy." This statement, however, does not consider important observations of the lithostratigraphic character and composition of the relevant transitional levels both at Bombrini and Mochi. It is well established that there is a considerable decrease in Mousterian artifacts in the upper spits of level IV at Bombrini and a considerable reduction in the area used to source the raw material found at the top of Unit I at Mochi. In addition, Bombrini records a semisterile phase in Upper level IV where only a few artifacts are present. In contrast, Mochi records sterile sediment in Unit H, as defined by Grimaldi et al. (2014). This might be due to worsening climatic conditions during the Neanderthal occupation at both sites, suggesting their presence was patchy and limited before the appearance of the first Proto-Aurignacian groups. We must, therefore, remain cautious of reaching broad conclusions regarding the dynamics of the Middle to Upper Paleolithic transition based on two neighboring sites. Instead, we must examine the situation in other parts of Italy.

At Fumane, a dolomitic limestone cave on a southern slope of the Venetian Pre-Alps (Fig. 1), the MP to UP transition involves not only late Mousterian and Proto-Aurignacian groups, as at Mochi, but also a transitional industry likened to the Uluzzian (Peresani et al., 2016). The appearance of the Uluzzian tools at Fumane

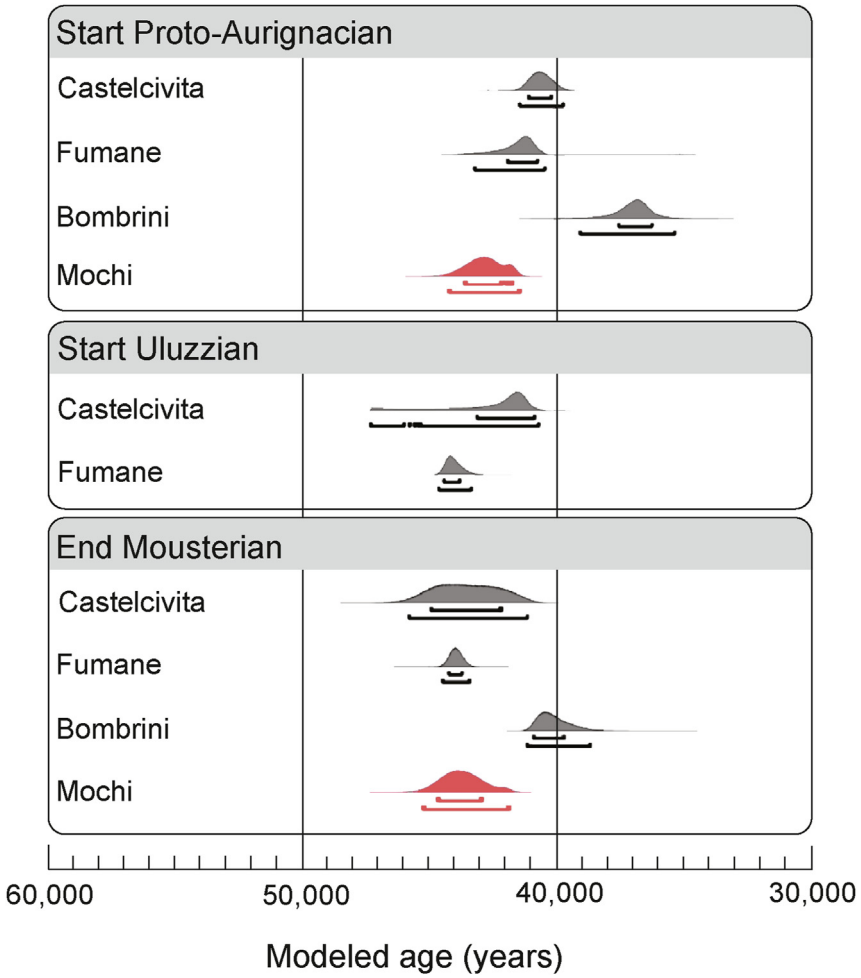

Figure 8. Bayesian model for the onset of the end of Mousterian, start of the Uluzzian, and start of the Proto-Aurignacian in northern Italy, using modeled chronometric data for Riparo Mochi (red), Bombrini, Fumane, and Castelcivita. (For interpretation of the references to color in this figure legend, the reader is referred to the Web version of this article).

represents a radical cultural change compared to the Mousterian. However, the assemblage also diverges from the classic Uluzzian profile from the southern Italian sites (Moroni et al., 2018; Villa et al., 2018; Peresani et al., 2019) and requires further reassessment. The latest Mousterian occurrences provide evidence of a well-structured use of living space, including areas with combustion structures such as fires and ash dumps and adjacent to areas used for Levallois flake manufacture. Tool shaping and curation, the use of bone tools, and butchering of ungulates and birds have also been identified in the uppermost MP units. The end of the Mousterian at Fumane was placed at 46–44 ka cal BP (95% probability; Higham et al., 2009). This age range is indistinguishable from the dates for the inferred Uluzzian at the site, which must have been a short-lived occupation. The start of the Proto-Aurignacian was placed at 43.2–40.4 ka cal BP (95% probability; Higham et al., 2009). Hence, the transition from the Mousterian to the Proto-Aurignacian is placed around 43 ka, an age estimate that is in the same range as the one we report here for Mochi.

Another important site in the south of Italy is the Castelcivita cave in Salerno (Fig. 1). The archaeological succession includes Mousterian, Uluzzian, and Proto-Aurignacian levels; the latter is sealed by thick volcanic deposits with the distinctive two-phase structure of the Campanian Ignimbrite (CI), therefore securely dating the end of the sequence at 39.85 ± 0.14 ka (Giaccio et al., 2017). The three lowermost MP levels at the site, currently undated, are capped by an erosional discontinuity that separates the Mousterian from the overlying Uluzzian deposits. The next three phases contain Proto-Aurignacian archaeological remains. The sequence was dated based on radiocarbon (Higham et al., 2014), with the end of the Mousterian being placed at 44.9–42.1 ka cal BP (68% probability) or between 45.8 and 41.1 ka cal BP (95% probability). The start of the Uluzzian remains undated, but it is constrained by a radiocarbon age from the top of the Uluzzian falling between 41.9 and 40.6 ka cal BP, with the CI pumice and gray ash capping the Proto-Aurignacian levels at 39.9 ka BP. Hence, we may also tentatively place the transition between 44 and 42 ka. A detailed dating program is currently targeting the MP part of the sequence. This will allow us to compare the Mousterian in the north further and the south of the Italian peninsula and better determine the timing of Neanderthal replacement.

Collectively, the new data we present here for the north of Italy agree with previous estimates for the timing of transition in Italy. At the sites of Mochi, Fumane, and Castelcivita, significant technological and cultural changes are observed in the millennia following 45 ka. During this time, the Mousterian tradition gave way to either the Uluzzian or the Proto-Aurignacian. The transition between the two had been completed at all these sites by the time the CI eruption made its mark in the sedimentary records of southern Italy. At sites such as Mochi, where the end of the Mousterian appears to be more gradual, we may hypothesize that late Neanderthal groups, if they were present, were sparse when modern human groups occupied the region and brought with them new technological and adaptive systems and cultural innovations. Finally, it is essential to point out the small number of Mousterian sites in Italy with available numerical ages and the need for more work in this region.

5. Conclusions

We present a comprehensive chronology for the MP sequence of Riparo Mochi, a site best known for preserving the various development stages of the UP. We show that Mousterian groups, likely Neanderthals, were at Riparo Mochi from the MIS 5 and continued to occupy the site over the MIS 3. The transition to the earliest UP at the site, whether represented by the start of Unit H or the beginning of Unit G, is dated between 44.3 and 41.1 ka (95.4% confidence level). These boundaries provide the best age estimate for the beginning of the Early UP and the establishment of modern human groups in the Balzi Rossi; the results also agree well with the emerging chronology from other sites in the north and the south of Italy. The Italian MP lacks chronometric precision, and several sites with long Mousterian sequences remain undated. We hope that developing an absolute chronometric framework for Riparo Mochi will highlight the need for more work and encourage systematic efforts toward understanding the chronology of the MP of the Italian Peninsula.

Acknowledgments

This research was supported by the European Research Council under the European Union's Seventh Framework Programme (FP7/2007e2013)/ERC grant agreement n°[324139] “PalaeoChron” awarded to T. Higham. We thank the staff of the Oxford Radiocarbon Accelerator Unit at the University of Oxford for support in the laboratory, particularly Dan Comeskey. A.K. Dave would like to thank the financial support provided by the Annual Fund and the Postgraduate Research Grant Scholarship from Brasenose College, University of Oxford during the 2015 fieldwork at Riparo Mochi.

Supplementary Online Material

Supplementary online material related to this article can be found at https://doi.org/10.1016/j.jhevol.2022.103211.

References

Aitken, M.J., 1998. Introduction to Optical Dating: The Dating of Quaternary Sediments by the Use of Photon-stimulated Luminescence. Clarendon Press, Oxford, UK.
Aitken, M.J., Xie, J., 1990. Moisture correction for annual gamma dose. Ancient TL 8, 6–9.
Alhaique, F., 2000. Risultati preliminari dell'analisi dei resti faunistici rinvenuti nei livelli del Paleolitico superiore di Riparo Mochi (Balzi Rossi): Scavi 1995e96. Atti del 2.
Anderson, L., Bon, F., Bordes, J.G., Pasquini, A., Slimak, L., Teyssandier, N., 2015. Relier des espaces, construire de nouveaux réseaux: Aux origines du Protoaurignacien et des débuts du Paléolithique supérieur en Europe occidentale. In: Les systèmes de mobilité de la Préhistoire au Moyen Âge. Actes des XXXVèmes Rencontres internationales d'archéologie et d'histoire d'Antibes, France, pp. 93–110.
Arellano, A., 2009. Les grands mammifères des niveaux moustériens de l'Abri Mochi (Grotte de Grimaldi, Ventimille, Italie). Fouilles de 1949. Bull. Mus. Anthropol. Préhist. Monaco. 49, 29–39.
Banks, W.E., d'Errico, F., Peterson, E.T., Kageyama, M., Sima, A., Sanchez-Goñi, M.F., 2008. Neanderthal extinction by competitive exclusion. PLoS One e3972.
Benazzi, S., Slon, V., Talamo, S., Negrino, F., Peresani, M., Bailey, S.E., Sawyer, S., Panetta, D., Vicino, G., Starnini, E., Mannino, M.A., Salvadori, P.A., Meyer, M., Pääbo, S., Hublin, J.-J., 2015. The makers of the Protoaurignacian and implications for Neandertal extinction. Science 348, 793–796.
Berto, C., Santaniello, F., Grimaldi, S., 2019. Palaeoenvironment and palaeoclimate in the western Liguria region (northwestern Italy) during the Last Glacial. The small mammal sequence of Riparo Mochi (Balzi Rossi, Ventimiglia). C. R. Palevol 18, 13–23.
Bietti, A., Boschian, G., Crisci, G.M., Danese, E., De Francesco, A.M., Dini, M., Fontana, F., Giampietri, A., Grifoni, R., Guerreschi, A., Liagre, J., Negrino, F., Radi, G., Tozzi, C., Tykot, R., 2004. Inorganic raw materials economy and provenance of chipped industry in some stone age sites of northern and central Italy. Coll. Antropol. 28, 41–54.
Bietti, A., Negrino, F., 2007. “Transitional” Industries from Neandertals to anatomically modern humans in Continental Italy: Present state of knowledge. In: Riel-Salvatore, J., Clark, G.A. (Eds.), New Approaches to the Study of Early Upper Paleolithic ‘Transitional' Industries in Western Eurasia. Archaeopress, Oxford, pp. 41–60.
Bird, M.I., Ayliffe, L.K., Fifield, L.K., Turney, C.S.M., Cresswell, R.G., Barrows, T.T., David, B., 1999. Radiocarbon dating of “old” charcoal using a wet oxidation, stepped-combustion procedure. Radiocarbon 41, 127–140.
Blanc, A.C., Cardini, L., Laplace, G., 1957-1961. Studio statistico delle industrie del Paleolitico superiore del Riparo Mochi ai Balzi Rossi di Grimaldi. Quaternaria V 340–355.
Bortolot, V.J., 2000. A new modular high capacity OSL reader system. Radiat. Meas. 32, 751–757.

Brock, F., Higham, T., Ditchfield, P., Bronk Ramsey, C., 2010. Current pretreatment methods for AMS radiocarbon dating at the Oxford Radiocarbon Accelerator Unit (Orau). Radiocarbon 52, 103–112.
Bronk Ramsey, C., 2009a. Bayesian analysis of radiocarbon dates. Radiocarbon 51, 337–360.
Bronk Ramsey, C., 2009b. Dealing with outliers and offsets in radiocarbon dating. Radiocarbon 51, 1023–1045.
Burow, C., 2020. calc_CentralDose( ): Apply the central age model (CAM) after Galbraith et al. (1999) to a given De distribution. Function version 1.4.0. In: Kreutzer, S., Burow, C., Dietze, M., Fuchs, M.C., Schmidt, C., Fischer, M., Friedrich, J. (Eds.), Luminescence: Comprehensive Luminescence Dating Data Analysis. R package version 0.9.7. https://CRAN.R-project.org/package=Luminescence.
Buylaert, J.P., Vandenberghe, D., Murray, A.S., Huot, S., De Corte, F., Van den Haute, P., 2007. Luminescence dating of old (>70ka) Chinese loess: A comparison of single-aliquot OSL and IRSL techniques. Quat. Geochronol. 2, 9–14.
Buylaert, J.P., Jain, M., Murray, A.S., Thomsen, K.J., Thiel, C., Sohbati, R., 2012. A robust feldspar luminescence dating method for Middle and Late Pleistocene sediments. Boreas 41, 435e451.
Combes, B., Philippe, A., Lanos, P., Mercier, N., Tribolo, C., Guerin, G., Guibert, P., Lahaye, C., 2015. A Bayesian central equivalent dose model for optically stimulated luminescence dating. Quat. Geochronol. 28, 62–70.
Conard, N.J., Bolus, M., 2003. Radiocarbon dating the appearance of modern humans and timing of cultural innovations in Europe: New results and new challenges. J. Hum. Evol. 44, 331–371.
Douka, K., 2017. 22. Radiocarbon dating of marine and terrestrial shell. In: Allen, M.J. (Ed.), Molluscs in Archaeology: Methods, Approaches and Applications, vol. 3. Oxbow Books, p. 200.
Douka, K., Hedges, R.E.M., Higham, T.F.G., 2010a. Improved AMS 14C dating of shell carbonates using high-precision X-Ray diffraction and a novel density separation protocol (CarDS). Radiocarbon 52, 735–751.
Douka, K., Higham, T.F.G., Hedges, R.E.M., 2010b. Radiocarbon dating of shell carbonates: Old problems and new solutions. Munibe Suplemento 31, 18–27.
Douka, K., Grimaldi, S., Boschian, G., del Lucchese, A., Higham, T.F.G., 2012. A new chronostratigraphic framework for the Upper Palaeolithic of Riparo Mochi (Italy). J. Hum. Evol. 62, 286–299.
Duller, G.A.T., 2003. Distinguishing quartz and feldspar in single grain luminescence measurements. Radiat. Meas. 37, 161–165.
Duller, G.A.T., 2018. Analyst v4.57 user manual. https://users.aber.ac.uk/ggd/analyst_manual_v4_57.pdf.
Duller, G.A.T., Tooth, S., Barham, L., Tsukamoto, S., 2015. New investigations at Kalambo Falls, Zambia: Luminescence chronology, site formation, and archaeological significance. J. Hum. Evol. 85, 111–125.
Durcan, J.A., King, G.E., Duller, G.A.T., 2015. DRAC: Dose rate and age calculator for trapped charge dating. Quat. Geochronol. 28, 54–61.
Frouin, M., Lahaye, C., Valladas, H., Higham, T., Debénath, A., Delagnes, A., Mercier, N., 2017. Dating the Middle Paleolithic deposits of La Quina Amont (Charente, France) using luminescence methods. J. Hum. Evol. 109, 30–45.
Galbraith, R.F., Roberts, R.G., Laslett, G.M., Yoshida, H., Olley, J.M., 1999. Optical dating of single and multiple grains of quartz from Jinmium rock shelter, northern Australia: PART I, experimental design and statistical models. Archaeometry 41, 339–364.
Giaccio, B., Hajdas, I., Isaia, R., Deino, A., Nomade, S., 2017. High-precision 14C and 40Ar/39Ar dating of the Campanian Ignimbrite (Y-5) reconciles the time-scales of climatic-cultural processes at 40 ka. Sci. Rep. 7, 45940.
Gliganic, L.A., Jacobs, Z., Roberts, R.G., Domínguez-Rodrigo, M., Mabulla, A.Z.P., 2012. New ages for Middle and Later Stone Age deposits at Mumba rockshelter, Tanzania: Optically stimulated luminescence dating of quartz and feldspar grains. J. Hum. Evol. 62, 533–547.
Godfrey-Smith, D.I., Huntley, D.J., Chen, W.-H., 1988. Optical dating studies of quartz and feldspar sediment extracts. Quat. Sci. Rev. 7, 373–380.
Grimaldi, S., Santaniello, F., 2014. New insights into Final Mousterian lithic production in western Italy. Quat. Int. 350, 116–129.
Grimaldi, S., Santaniello, F., 2020. What tools do we need to colonize Italy? The Early Protoaurignacian and the Noaillian Gravettian lithic evidence. In: Gibaja, J.F., Marreiros, J. (Eds.), Hunter-Gatherers' Tool-Kit: A Functional Perspective. Cambridge Scholars Publishing, Cambridge, pp. 62–78.
Grimaldi, S., Porraz, G., Santaniello, F., 2014. Raw material procurement and land use in the northern Mediterranean Arc: Insight from the first Proto-Aurignacian of Riparo Mochi (Balzi Rossi, Italy). Quartär 61, 113–127.
Grimaldi, S., Santaniello, F., Starnini, E., 2017. Le Riparo Mochi (Balzi Rossi, Ventimiglia, Italie): Les nouvelles fouilles. Bull. Soc. Préhist. Française 114, 169–172.
Guérin, G., Mercier, N., Adamiec, G., 2011. Dose-rate conversion factors: Update. Ancient TL 29, 5–8.
Guérin, G., Discamps, E., Lahaye, C., Mercier, N., Guibert, P., Turq, A., Dibble, H.L., McPherron, S.P., Sandgathe, D., Goldberg, P., Jain, M., Thomsen, K., Patou-Mathis, M., Castel, J.-C., Soulier, M.-C., 2012a. Multi-method (TL and OSL), multi-material (quartz and flint) dating of the Mousterian site of Roc de Marsal (Dordogne, France): Correlating Neanderthal occupations with the climatic variability of MIS 5–3. J. Archaeol. Sci. 39, 3071–3084.
Guérin, G., Mercier, N., Nathan, R., Adamiec, G., Lefrais, Y., 2012b. On the use of the infinite matrix assumption and associated concepts: A critical review. Radiat. Meas. 47, 778–785.
Guérin, G., Christophe, C., Philippe, A., Murray, A.S., Thomsen, K.J., Tribolo, C., Urbanova, P., Jain, M., Guibert, P., Mercier, N., Kreutzer, S., Lahaye, C., 2017. Absorbed dose, equivalent dose, measured dose rates, and implications for OSL age estimates: Introducing the Average Dose Model. Quat. Geochronol. 41, 163–173.
Heathon, T.J., Köhler, P., Butzin, M., Bard, E., Reimer, R.W., Austin, W.E.N., Bronk Ramsey, C., Grootes, P.M., Hughen, K.A., Kromer, B., Reimer, P.J., Adkins, J., Burke, A., Cook, M.S., Olsen, J., Skinner, L.C., 2020. Marine20—The marine radiocarbon age calibration curve (0–55,000 calBP). Radiocarbon 62, 779–820.
Hedges, J.I., Cowie, G.L., Richey, J.E., Quay, P.D., Benner, R., Strom, M., Forsberg, B.R., 1994. Origins and processing of organic matter in the Amazon River as indicated by carbohydrates and amino acids. Limnol. Oceanogr. 39, 743–761.
Heydari, M., Guérin, G., 2018. OSL signal saturation and dose rate variability: Investigating the behaviour of different statistical models. Radiat. Meas. 120, 96–103.
Higham, T., Brock, F., Peresani, M., Broglio, A., Wood, R., Douka, K., 2009. Problems with radiocarbon dating the Middle to Upper Palaeolithic transition in Italy. Quat. Sci. Rev. 28, 1257–1267.
Higham, T., Douka, K., Wood, R., Bronk Ramsey, C., Brock, F., Basell, L., Camps, M., Arrizabalaga, A., Baena, J., Barroso-Ruíz, C., Bergman, C., Boitard, C., Boscato, P., Caparrós, M., Conard, N.J., Draily, C., Froment, A., Galván, B., Gambassini, P., Garcia-Moreno, A., Grimaldi, S., Haesaerts, P., Holt, B., Iriarte-Chiapusso, M.-J., Jelinek, A., Jordá Pardo, J.F., Maíllo-Fernández, J.-M., Marom, A., Maroto, J., Menéndez, M., Metz, L., Morin, E., Moroni, A., Negrino, F., Panagopoulou, E., Peresani, M., Pirson, S., de la Rasilla, M., Riel-Salvatore, J., Ronchitelli, A., Santamaria, D., Semal, P., Slimak, L., Soler, J., Soler, N., Villaluenga, A., Pinhasi, R., Jacobi, R., 2014. The timing and spatiotemporal patterning of Neanderthal disappearance. Nature 512, 306–309.
Huntley, D.J., Baril, M.R., 1997. The K content of the K-feldspars being measured in optical dating or in thermoluminescence dating. Ancient TL 11–13.
Huntley, D.J., Hancock, R., Ancient, T.L., 2001. The Rb contents of the K-feldspar grains being measured in optical dating. Ancient TL 19, 43–46.
Jain, M., Ankjaergaard, C., 2011. Towards a non-fading signal in feldspar: Insight into charge transport and tunnelling from time-resolved optically stimulated luminescence. Radiat. Meas. 46, 292–309.
Khatib, S., Ivaldi, J.-P., Onoratini, G., Lumley, H. de, Bietti, A., 2012. Contribution de la minéralogie des sables à l'étude des paléoenvironnements du moustérien et du paléolithique supérieur de l'abri Mochi (Ligurie italienne). Quaternaire 23, 49–60.
Klasen, N., Kehl, M., Mikdad, A., Brückner, H., Weniger, G.-C., 2017. Chronology and formation processes of the Middle to Upper Palaeolithic deposits of Ifri n'Ammar using multi-method luminescence dating and micromorphology. Quat. Int. 485, 89–102.
Kreutzer, S., Schmidt, C., Fuchs, M.C., Dietze, M., Fischer, M., Fuchs, M., 2012. Introducing an R package for luminescence dating analysis. Ancient TL 30, 1–8.
Kreutzer, S., Martin, L., Guérin, G., Tribolo, C., Selva, P., Mercier, N., 2019. Environmental dose rate determination using a passive dosimeter: Techniques and workflow for alpha-Al2O3:C chips. Geochronometria 45, 56–67.
Kreutzer, S., Burow, C., Dietze, M., Fuchs, M., Schmidt, C., Fischer, M., Friedrich, J., 2020. Luminescence: comprehensive luminescence dating data analysis. R package version 0.9.7. https://CRAN.R-project.org/package=Luminescence.
Kuhn, S.L., Bietti, A., 2000. The Late Middle and early Upper Paleolithic in Italy. In: Bar-Yosef, O., Pilbeam, D. (Eds.), The Geography of Neandertals and Modern Humans in Europe and the Greater Mediterranean, Peabody Mus. Bull., Vol. 8. Harvard University, Peabody Mus. Archaeol. Ethnol, pp. 49–76.
Kuhn, S.L., Stiner, M.C., 1992. New research on Riparo Mochi, Balzi Rossi (Liguria): Preliminary results. Quat. Nova 11, 79–90.
Kuhn, S.L., Stiner, M.C., 1998. Reports The Earliest Aurignacian of Riparo Mochi (Liguria, Italy). Curr. Anthropol. 39, S175–S189.
Laplace, G., 1977. Il riparo Mochi ai Balzi Rossi di Grimaldi (fouilles 1938-1949). Les industries leptolithiques. Riv. Sci. Preist. 32 (1–2), 3–131.
Mercier, N., Valladas, H., Valladas, G., Reyss, J.-L., Joron, J.-L., 1994. A new dosimetric calibration tool. Radiat. Meas. 23, 507–508.
Moroni, A., Ronchitelli, A., Arrighi, S., Aureli, D., 2018. Grotta del Cavallo (Apulia—Southern Italy). The Uluzzian in the mirror. J. Anthropol. Sci. 96, 125–160.
Murray, A.S., Wintle, A.G., 2003. The single aliquot regenerative dose protocol: Potential for improvements in reliability. Radiat. Meas. 37, 377–381.
Murray, A.S., Wintle, A.G., 2000. Luminescence dating of quartz using an improved single-aliquot regenerative-dose protocol. Radiat. Meas. 32, 57–73.
Murray, A.S., Thomsen, K.J., Masuda, N., Buylaert, J.P., Jain, M., 2012. Identifying well-bleached quartz using the different bleaching rates of quartz and feldspar luminescence signals. Radiat. Meas. 47, 688–695.
Palma di Cesnola, A., 1993. Il Paleolitico Superiore in Italia: Introduzione Allo Studio. Garlatti e Razzai, Firenze.
Peresani, M., Cristiani, E., Romandini, M., 2016. The Uluzzian technology of Grotta di Fumane and its implication for reconstructing cultural dynamics in the Middle–Upper Palaeolithic transition of Western Eurasia. J. Hum. Evol. 91, 36–56.
Peresani, M., Bertola, S., Delpiano, D., Benazzi, S., Romandini, M., 2019. The Uluzzian in the north of Italy. Insights around the new evidence at Riparo Broion Rockshelter. Archaeol. Anthropol. Sci. 11, 3503–3536.
Porraz, G., Negrino, F., 2008. Espaces économiques et approvisionnement minéral au Paléolithique moyen dans l'aire Liguro-Provençale. Bull. Mus. Anthropol. Préhist. Monaco 1, 29–39.
Porraz, G., Simon, P., Pasquini, A., 2010. Identité technique et comportements économiques des groupes proto-aurignaciens à la grotte de l'Observatoire (principauté de Monaco). Gallia Préhist 52, 33–59.

Prescott, J.R., Hutton, J.T., 1994. Cosmic ray contributions to dose rates for luminescence and ESR dating: Large depths and long-term time variations. Radiat. Meas. 23, 497–500.
R Core Team, R.C., 2020. R: A language and environment for statistical computing. R foundation for statistical computing, Vienna.
Reimer, P.J., Austin, W.E.N., Bard, E., Bayliss, A., Blackwell, P.G., Bronk Ramsey, C., Butzin, M., Cheng, H., Edwards, R.L., Friedrich, M., Grootes, P.M., Guilderson, T.P., Hajdas, I., Heaton, T.J., Hogg, A.G., Hughen, K.A., Kromer, B., Manning, S.W., Muscheler, R., Palmer, J.G., Pearson, C., van der Plicht, J., Reimer, R.W., Richards, D.A., Scott, E.M., Southon, J.R., Turney, C.S.M., Wacker, L., Adolphi, F., Büntgen, U., Capano, M., Fahrni, S.M., Fogtmann-Schulz, A., Friedrich, R., Köhler, P., Kudsk, S., Miyake, F., Olsen, J., Reinig, F., Sakamoto, M., Sookdeo, A., Talamo, S., 2020. The IntCal20 northern hemisphere radiocarbon age calibration curve (0-55 cal kBP). Radiocarbon 62, 725–757.
Reimer, P.J., McCormac, F.G., 2002. Marine radiocarbon reservoir corrections for the Mediterranean and Aegean Seas. Radiocarbon 44, 159–166.
Richter, D., Pintaske, R., Dornich, K., Krbetschek, M., 2012. A novel beta source design for uniform irradiation in dosimetric applications. Ancient TL 30, 57–63.
Richter, D., Richter, A., Dornich, K., 2013. Lexsyg—A new system for luminescence research. Geochronometria 40, 220–228.
Rossoni-Notter, E., Notter, O., Simone, S., Simon, P., 2016. Acheulean breccias of Prince cave (Liguria, Italy): New insights and regional issues. Quat. Int. 411, 236–253.
Santaniello, F., 2016. Il Gravettiano dell'Italia tirrenica nel contesto mediterraneo: Definizione delle strategie di insediamento e mobilità attraverso lo studio delle materie prime e delle industrie litiche. Ph.D. Dissertation University of Trento.
Santaniello, F., Grimaldi, S., 2019. Le Gravettien entre l'Italie et la France: Nouvelles données sur l'industrie lithique de l'Abri Mochi (Balzi Rossi, Italie). Bull. Soc. Préhist. Française 116, 255–282.
Santaniello, F., Grimaldi, S., 2020. A techno-functional interpretation of the Noailles burins from the Riparo Mochi (Balzi Rossi, Italy). Quat. Int. 587–588, 75–85.
Smedley, R.K., Duller, G.A.T., Roberts, H.M., 2015. Bleaching of the post-IR IRSL signal from individual grains of K-feldspar: Implications for single-grain dating. Radiat. Meas. 79, 33–42.
Smith, F.H., Janković, Karavanić, I., 2005. The assimilation model, modern human origins in Europe, and the extinction of Neandertals. Quat. Int. 137, 7–19.
Stiner, M.C., 1999. Palaeolithic mollusc exploitation at Riparo Mochi (Balzi Rossi, Italy): Food and ornaments from the Aurignacian through Epigravettian. Antiquity 73, 735–754.
Tagliacozzo, A., Zeppieri, F., Fiore, I., Spinapolice, E., 2012. Archaeozoological evidence of subsistence strategies during the Gravettian at Riparo Mochi (Balzi Rossi, Ventimiglia, Imperia-Italy). Quat. Int. 252, 142–154.
Tejero, J.-M., Grimaldi, S., 2015. Assessing bone and antler exploitation at Riparo Mochi (Balzi Rossi, Italy): Implications for the characterization of the Aurignacian in South-western Europe. J. Archaeol. Sci. 61, 59–77.
Thiel, C., Buylaert, J.P., Murray, A., Terhorst, B., Hofer, I., Tsukamoto, S., Frechen, M., 2011. Luminescence dating of the Stratzing loess profile (Austria)—testing the potential of an elevated temperature post-IR IRSL protocol. Quat. Int. 234, 23–31.
Thomsen, K.J., Murray, A.S., Jain, M., Bøtter-Jensen, L., 2008. Laboratory fading rates of various luminescence signals from feldspar-rich sediment extracts. Radiat. Meas. 43, 1474–1486.
Timmermann, A., 2020. Quantifying the potential causes of Neanderthal extinction: Abrupt climate change versus competition and interbreeding. Quat. Sci. Rev. 238, 106331.
Tomasso, A., 2014. Territoires, systèmes de mobilité et systèmes de production. La fin du Paléolithique supérieur dans l'arc liguro-provençal. Bull. Soc. Préhist. Française 111, 748–749.
Vaesen, K., Scherjon, F., Hemerik, L., Verpoorte, A., 2019. Inbreeding, Allee effects and stochasticity might be sufficient to account for Neanderthal extinction. PLoS One 14, e0225117.
Villa, P., Pollarolo, L., Conforti, J., Marra, F., Biagioni, C., Degano, I., et al., 2018. From Neandertals to modern humans: New data on the Uluzzian. PLoS One 13, e0196786.
Wintle, A.G., 1997. Luminescence dating: Laboratory procedures and protocols. Radiat. Meas. 27, 769–817.
Wintle, A.G., Murray, A.S., 2006. A review of quartz optically stimulated luminescence characteristics and their relevance in single-aliquot regeneration dating protocols. Radiat. Meas. 41, 369–391.
Wood, R.E., Douka, K., Boscato, P., Haesaerts, P., Sinitsyn, A., Higham, T.F.G., 2012. Testing the ABOx-SC method: Dating known-age charcoals associated with the Campanian Ignimbrite. Quat. Geochronol. 9, 16–26.